Geochemistry Geophysics Geosystems G3

*Article*
Volume 14, Number XX
31 July 2013
doi: 10.1002/ggge.20168
ISSN: 1525-2027

Published by AGU and the Geochemical Society

# Relating sulfate and methane dynamics to geology: Accretionary prism offshore SW Taiwan

**Pei-Chuan Chuang**
*Department of Geosciences, National Taiwan University, Taipei, Taiwan*

*Now at Institute of Marine Sciences, University of California, Santa Cruz, California, USA*

**Andrew W. Dale, Klaus Wallmann, and Matthias Haeckel**
*Helmholtz Centre for Ocean Research Kiel (GEOMAR), Kiel, Germany*

**Tsanyao Frank Yang, Nai-Chen Chen, Hsiao-Chi Chen, and Hsuan-Wen Chen**
*Department of Geosciences, National Taiwan University, No. 1, Sec. 4, Roosevelt Road , Taipei 106, Taiwan (tyyang@ntu.edu.tw)*

**Saulwood Lin**
*Institute of Oceanography, National Taiwan University, Taipei, Taiwan*

**Chih-Hsien Sun**
*Exploration and Development Research Institute, CPC Corporation, Miaoli, Taiwan*

**Chen-Feng You**
*Department of Earth Sciences, National Cheng Kung University, Tainan City, Taiwan*

**Chorng-Shern Horng**
*Institute of Earth Sciences, Academia Sinica, Nangang, Taipei, Taiwan*

**Yunshuen Wang and San-Hsiung Chung**
*Central Geological Survey, MOEA, New Taipei City, Taiwan*

[1] Geochemical data ($CH_4$, $SO_4^{2-}$, $I^-$, $Cl^-$, particulate organic carbon (POC), $\delta^{13}C$-$CH_4$, and $\delta^{13}C$-$CO_2$) are presented from the upper 30 m of marine sediment on a tectonic submarine accretionary wedge offshore southwest Taiwan. The sampling stations covered three ridges (Tai-Nan, Yung-An, and Good Weather), each characterized by bottom simulating reflectors, acoustic turbidity, and different types of faulting and anticlines. Sulfate and iodide concentrations varied little from seawater-like values in the upper 1–3 m of sediment at all stations; a feature that is consistent with irrigation of seawater by gas bubbles rising through the soft surface sediments. Below this depth, sulfate was rapidly consumed within 5–10 m by anaerobic oxidation of methane (AOM) at the sulfate-methane transition. Carbon isotopic data imply a mainly biogenic methane source. A numerical transport-reaction model was used to identify the supply pathways of methane and estimate depth-integrated turnover rates at the three ridges. Methane gas ascending from deep layers, facilitated by thrusts and faults, was by far the dominant term in the methane budget at all sites.

Differences in the proximity of the sampling sites to the faults and anticlines mainly accounted for the variability in gas fluxes and depth-integrated AOM rates. By comparison, methane produced in situ by POC degradation within the modeled sediment column was unimportant. This study demonstrates that the geochemical trends in the continental margins offshore SW Taiwan are closely related to the different geological settings.

**Components:** 15,138 words, 6 figures, 6 tables.

**Keywords:** gas hydrate; methane flux; bubble irrigation; anaerobic oxidation of methane; POC degradation; accretionary wedge; Taiwan.

**Index Terms:** 0414 Biogeochemical cycles, processes, and modeling: Biogeosciences; 0412 Biogeochemical kinetics and reaction modeling: Biogeosciences; 3004 Gas and hydrate systems: Marine Geology and Geophysics.

**Received** 4 October 2012; **Revised** 1 May 2013; **Accepted** 2 May 2013; **Published** 31 July 2013.

Chuang, P.-C., A. W. Dale, K. Wallmann, M. Haeckel, T. F. Yang, N.-C. Chen, H.-C. Chen, H.-W. Chen, S. Lin, C.-H. Sun, C.-F. You, C.-S. Horng, Y. Wang, and S.-H. Chung (2013), Relating sulfate and methane dynamics to geology: Accretionary prism offshore SW Taiwan, *Geochem. Geophys. Geosyst.*, *14*, 2523–2545, doi:10.1002/ggge.20168.

## 1. Introduction

[2] Gas hydrates are typically composed of natural gas, mainly methane ($CH_4$), within a rigid lattice of water molecules and form an important reservoir in the global carbon cycle [*Kvenvolden*, 1993, 1998; *Dickens*, 2001; *Milkov*., 2004]. In the marine environment, hydrates usually occur under conditions of low temperature and moderate pressure such as continental slope sediments [*Kvenvolden*, 1993]. The presence of gas hydrates can be inferred by a bottom simulating reflector (BSR) that identifies the acoustic contrast between hydrate-bearing sediment and the free gas in the pore space below, i.e., the lower boundary of the gas hydrate stability zone [*Hyndman and Davis*, 1992; *Holbrook et al*., 1996].

[3] BSRs have been detected in the area offshore southwestern Taiwan in the collision zone between the Luzon Arc of the Philippine Sea and Eurasian continental plates [*Chi et al*., 1998; *Liu et al*., 2006]. An active accretionary prism is formed by the collision and a deformation front separating the distinctive fold-and-thrust structures of the convergent zone and horst-and-graben structures of the passive margin. Changes of geothermal gradients due to arc-continental collision may affect gas hydrate stability and determine the extent to which gas can be transported from below the BSR upward along thrusts and faults [*Lin et al*., 2008; *C. C. Lin et al*., 2009]. Gassy sediments, diapirs, and mud volcanoes observed on land and offshore SW Taiwan demonstrate that fluids and methane ascend along faults from deep sediments to the surface [*Yang et al*., 2003, 2004; *You et al*., 2004; *Yeh et al*., 2005; *Chiu et al*., 2006; *Sun et al*., 2010].

[4] The aforementioned geophysical features are supported by previous geochemical observations that suggest a highly active methane cycle in the overlying sediments offshore SW Taiwan. These include high methane and sulfide fluxes, high rates of sulfate reduction, extremely depleted carbon isotope values of authigenic carbonates, and occurrences of pyrite tubes in cored sediments [*Chuang et al*., 2006, 2010; *Lin et al*., 2006; *Huang et al*., 2006; *Yang et al*., 2006; *Yang*, 2008; *Lim et al*., 2011]. Ongoing methanogenesis and methane transport from below the BSR generate a flux of dissolved and gaseous methane directed upward toward the sea floor, although there is lack of geochemical data indicating upward fluid advection. The dissolved methane fraction does not reach the ocean water, however, since it is consumed in situ by microorganisms that respire the methane anaerobically using sulfate as the electron acceptor [*Barnes and Goldberg*, 1976]. Anaerobic oxidation of methane (AOM) takes place in the sulfate-methane transition (SMT) zone where sulfate and methane

become almost completely consumed, and where sulfide is produced as a metabolic waste product. Upward diffusion and oxidation of sulfide can supply large amounts of energy to chemosynthetic benthic communities living on and within the sea floor [*Suess et al*., 1985; *Treude et al*., 2003; *Dale et al*., 2010].

[5] The amount of sedimentary methane in the upper sediment layers is determined by the relative rates of dissolved and gaseous methane migration from deep sediment layers through diffusion and advection, methanogenesis, and AOM. Sulfate profiles at several sites offshore Taiwan presented by *Chuang et al*. [2010] reveal pore water sulfate concentrations remaining at bottom water values from the sediment surface down to over 3 m below seafloor (mbsf). These geochemical signatures have been explained by nonlocal transport of solutes in other active [*Haeckel et al*., 2007] and passive margin sediments [*Fossing et al*., 2000]. One such process, bubble irrigation, describes the exchange of pore water with overlying seawater driven by gas bubbles rising through the sediment [*Haeckel et al*., 2007]. Observations of gas plumes from the sea floor offshore SW Taiwan [*S. Lin et al*., 2009] provide further indications for bubble release to the water column. Additional evidence for seafloor gas escape is inferred from higher methane and helium concentrations in the bottom water and in the water column [*Suess et al*., 1999; *Chuang et al*., 2006; *Yang et al*., 2006].

[6] The main objective of this study is to report how the contrasting geology of three tectonically active ridges offshore SW Taiwan (Yung-An, Tai-Nan, and Good Weather ridges) modulates the major geochemical features in the upper 30 m of sediments. A numerical transport-reaction model established previously by *Wallmann et al*. [2006a] is applied to a suite of measured geochemical data to identify and quantify the diagenetic processes controlling methane, sulfate, and particulate organic carbon (POC) turnover at each site. The derived fluxes and depth-integrated rates are discussed in relation to the different tectonic structures of the ridges. Headspace carbon isotopic data of methane ($\delta^{13}$C-$CH_4$) and carbon dioxide ($\delta^{13}$C-$CO_2$) are also presented to provide additional information on the origin of methane.

## 2. Study Area

[7] The region offshore southwestern Taiwan is located at the northern end of the South China Sea between the subducting Eurasian plate and the overriding Philippine Sea plate. The main tectonic structures of the accretionary wedge and the passive continental margin, separated by the deformation front, form in this area. Different fault systems develop on each side of the deformation front. The passive Chinese continental margin lies on the western side where normal faults form horsts and grabens, whereas a series of imbricated thrusts and folds in the accretionary wedge lie to the east [*Liu et al*., 1997]. The amount of strata that was uplifted and compressed when the South China Sea lithosphere subducted eastward under the Luzon Arc during the Cenozoic decreases from east to west up to the deformation front. The Manila Trench, North Luzon Arc, North Luzon Trough, and Hengchun Ridge are located in this area with a north-south orientation [*Teng*, 1990; *Huang et al*., 1997; *Liu et al*., 1998]. The regional lineament structures, such as Kaoping Canyon, Penghu Canyon, Shoushan Ridge, and Tainan Ridge, are also characterized by a north-south trend due to the eastward subduction and collision [*Liu et al*., 2004].

[8] *Reed et al*. [1992] defined upper and lower slope areas of the accretionary wedge offshore SW Taiwan. The former consists of thrust faults/fractures that may provide potential pathways for deep fluid migration that ultimately form mud volcanoes. According to seismic image analysis [*Liu et al*., 1997; *Lin et al*., 2008; *C.C. Lin et al*., 2009], the lower slope, where the ridges studied in this manuscript are located, can be further divided into rear segments and frontal segments (Figure 1). In the frontal segment, between the deformation front and the rear segment, anticline and blind thrust faults (faults do not cut through shallow strata and break through the seafloor) are two dominant structures. Tai-Nan Ridge, which is representative of this tectonic setting, lies in the frontal segment. Yung-An Ridge and Good Weather Ridge are located in the rear segment where emergent thrust faults (those that penetrate strata and break the seafloor) dominate the ridges [*Lin et al*., 2008; *C.C. Lin et al*., 2009]. Seismic and TowCam surveys of the seafloor have shown that the entire area is characterized by pockmarks, gas chimneys and plumes, authigenic carbonates, and acoustic turbidity [*Chiu et al*., 2006; Lin et al., unpublished data].

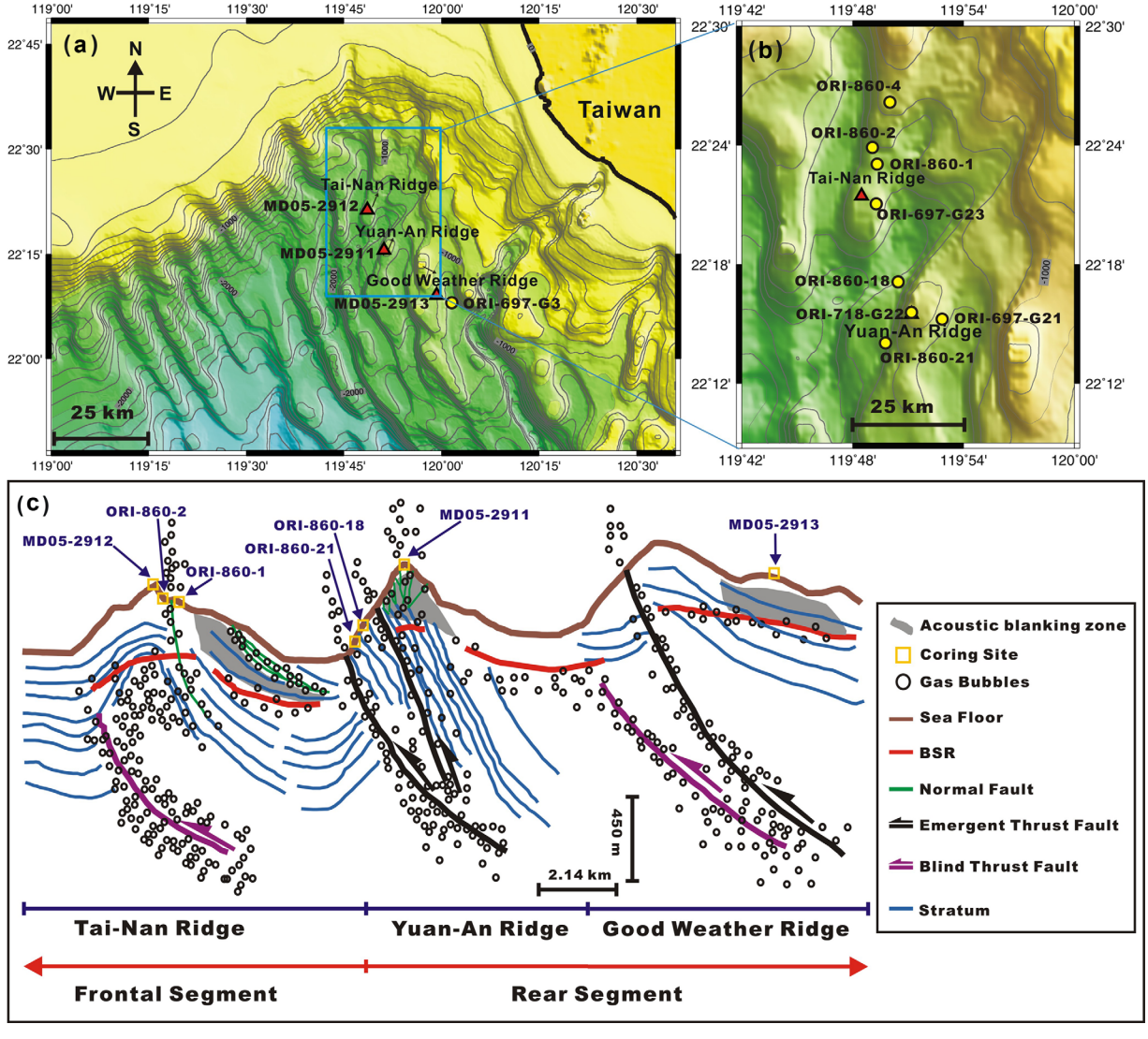


**Figure 1.** (a) Bathymetry of the shelf and slope off southwestern Taiwan showing the three *Marion Dufresne (MD)* coring sites (red triangles), one additional ORI site (yellow circle), and locations of Tai-Nan Ridge, Yung-An Ridge, and Good Weather Ridge. (b) Enlargement showing the four main *Ocean Researcher I (ORI)* coring sites (yellow circles) where pore water geochemistry was measured as well as four additional ORI sites (yellow circles) where supporting data was collected (Table 1). (c) Schematic cross section of the upper portion of the accretionary wedge through the three ridges drawn from seismic lines MCS647, MCS681, and MCS716 (modified from *Lin et al*. [2008]). The stations indicated are those shown in Figure 2. The presence of gas bubbles is inferred from seismic data and from observed gas plumes in the water column.

## 3. Sampling Sites

[9] The diagenetic model is applied to data from Tai-Nan Ridge, Yung-An Ridge and Good Weather Ridge where preliminary geochemical and geophysical characteristics have been reported previously [*Chuang et al*., 2006, 2010; *Huang et al*., 2006; *Lin et al*., 2006; *Liu et al*., 2006; *Yang et al*., 2006; *Yang*, 2008]. Long piston cores were recovered at three sites (MD05-2911, MD05-2912, and MD05-2913) from the lower slope during Leg 2 of *MD147/MARCO POLO 1/IMAGES XII* cruise of R/V *Marion Dufresne* (MD) in May and June 2005. Sites MD05-2911, MD05-2912, and MD05-2913 are situated on Yung-An Ridge, Tai-Nan Ridge, and Good Weather Ridge, respectively (Figure 1a and Table 1). These are referred to as MD cores/sites in the text. Data from four short piston cores (~5 m) sampled with R/V *Ocean Researcher I* (ORI-860) in 2008 are also presented (Figure 1b

**Table 1.** Sampling Locations and Piston Core Recovery Lengths

| Sites/Cores | Latitude (N) | Longitude (E) | Water Depth (m) | Core Length (m) |
|---|---|---|---|---|
| MD05–2911 | 22°15.62′ | 119°51.08′ | 1076 | 24.00 |
| MD05–2912 | 22°21.50′ | 119°48.50′ | 1093 | 30.50 |
| MD05–2913 | 22°9.156′ | 119°59.28′ | 1095 | 12.60 |
| ORI-860-1 | 22°23.15′ | 119°49.48′ | 1186 | 3.90 |
| ORI-860-2 | 22°23.91′ | 119°49.31′ | 1158 | 3.99 |
| ORI-860-18 | 22°17.25′ | 119°50.48′ | 1442 | 4.01 |
| ORI-860-21 | 22°14.11′ | 119°49.70′ | 1472 | 4.51 |
| ORI-860-4[a] | 22°26.28′ | 119°49.88′ | 962 | 4.20 |
| ORI-697-G23[b] | 22°21.17′ | 119°48.87′ | 1228 | 4.35 |
| ORI-718-G22[c] | 22°15.61′ | 119°51.08′ | 1104 | 4.58 |
| ORI-697-G3[d] | 22°08.57′ | 120°01.55′ | 1363 | 3.08 |
| ORI-697-G21[d] | 22°15.29′ | 119°52.88′ | 1276 | 3.49 |

[a]Reference site for chloride data.
[b]POC data from this core is plotted in Figure 2 for Tai-Nan Ridge.
[c]POC data from this core is plotted in Figure 2 for Yung-An Ridge.
[d]Cores used for carbon-14 dating.

and Table 1). Cores ORI-860-1 and ORI-860-2 were recovered from Tai-Nan Ridge and cores ORI-860-18 and ORI-860-21 were recovered from Yung-An Ridge. These are referred to as the ORI cores/sites in the text. Due to a lack of sediment samples for POC analysis at these ORI sites, POC was analyzed in two additional cores sampled on Tai-Nan Ridge (station ORI-697-G23) and Yung-An Ridge (station ORI-718-G22). Sediments from two additional cores (ORI-697-G21 and ORI-697-G3) were used for carbon-14 dating. As a reference for chloride concentrations, Site ORI-860-4 was sampled on Tai-Nan Ridge. The upper 30 m of sediments cored all lie within the gas hydrate stability zone. A schematic of the main geological features including the BSR and areas of acoustic turbidity is shown in Figure 1c.

## 4. Analytical Methods

[10] Bottom water temperature and salinity (conductivity) data for three ridges (Table 2) were obtained by a Seabird-25 CTD mounted on the TowCam system during cruise *OR1–768* in 2005 (Lin et al., unpublished data).

[11] After core retrieval onboard, sediment sections (3–10 cm long) were subsampled at 25 cm (ORI sites) and 50 cm (MD sites) intervals. Wet sediment samples were split into three parts for analysis of gas ($CH_4$, $\delta^{13}$C-$CH_4$, and $\delta^{13}$C-$CO_2$), pore water chemistry ($SO_4^{2-}$, $Cl^-$, and $I^-$), POC content, and porosity.

### 4.1. Gas Analysis

[12] Sediment for methane gas determination was transferred immediately into 20 mL glass vials filled with a saturated NaCl solution to inhibit microbiological activity and decrease the gas solubility [*Milkov*, 2004]. The vials were sealed with butyl rubber stoppers and capped with aluminum crimps. Before analysis, 5 mL of NaCl solution was removed and replaced by the same volume of pure nitrogen gas as the headspace. Afterward, the sample vials were shaken and placed in an ultrasonic bath for 30 min at room temperature (25°C). Three milliliters of gas was removed from the headspace with a syringe for analysis and the same volume of NaCl solution was injected to replace the volume of the gas removed.

[13] Gas was introduced into a gas chromatograph (GC) (SRI 8610C) equipped with both thermal conductivity (TCD) and flame ionization (FID) detectors (injection temperature 30°C, held isothermal for 2 min, ramped to 250°C at 120°C/min). Hydrogen and argon were used as carrier gases. Hydrogen was supplied by a hydrogen generator for use in the FID and in one TCD; argon supplied by a cylinder tank was used in another TCD. In general, most gas components analyzed in this system have analytical errors less than 5% with low detection limits [*Chuang et al.*, 2010; *Lee et al.*, 2005, 2008].

[14] Carbon isotopic ratios were measured using a Finnigan Delta-PlusXL isotope ratio mass spectrometer with a HP 5890 gas chromatograph and a combustion III interface. For the measurement of the $^{13}C/^{12}C$ ratio, $CH_4$ and $CO_2$ were separated with a GS-Q fused silica column and quantitatively converted to $CO_2$ and $H_2O$ by passage through a Pt-Cu-Ni combustion reactor at 940°C. Carbon-stable isotope ratios are expressed in the conventional delta ($\delta$) notation and reported relative to the international standards of Vienna Peedee

**Table 2.** Imposed Parameters and Boundary Conditions Used in the Model for Each Site/Ridge

| | Tai-Nan | | | Yung-An | | | Good Weather |
|---|---|---|---|---|---|---|---|
| | MD05–2912 | ORI-860-1 | ORI-860-2 | MD05–2911 | ORI-860-18 | ORI-860-21 | MD05–2913 |
| Temperature ($T$, °C) | 3.5 | 3.5 | 3.5 | 3.5 | 3.5 | 3.5 | 3.5 |
| Salinity | 34.6 | 34.6 | 34.6 | 34.6 | 34.6 | 34.6 | 34.6 |
| Pressure at seafloor ($P$, MPa) | 11.4 | 12.1 | 11.8 | 11.2 | 14.6 | 14.9 | 11.2 |
| Sediment porosity at zero depth ($\Phi_0$) | 0.68 | 0.56 | 0.54 | 0.86 | 0.65 | 0.67 | 0.68 |
| Sediment porosity in compacted sediments ($\Phi_f$) | 0.631 | 0.40 | 0.45 | 0.58 | 0.4 | 0.54 | 0.55 |
| Depth attenuation coefficient of porosity ($p$, $cm^{-1}$) | 1/460 | 1/460 | 1/460 | 1/460 | 1/460 | 1/460 | 1/460 |
| Sediment burial velocity ($w_f$, cm $yr^{-1}$) | 0.04 | 0.04 | 0.04 | 0.04 | 0.04 | 0.04 | 0.08 |
| Molecular diffusion coefficient for $SO_4^{2-}$ ($D_m$, $cm^2$ $yr^{-1}$) | 180 | 180 | 180 | 180 | 180 | 180 | 180 |
| Molecular diffusion coefficient for $CH_4$ ($D_m$, $cm^2$ $yr^{-1}$) | 294 | 294 | 294 | 294 | 294 | 294 | 294 |
| Molecular diffusion coefficient for $I^-$ ($D_m$, $cm^2$ $yr^{-1}$) | 357 | 357 | 357 | 357 | 357 | 357 | 357 |
| Equilibrium concentration for dissolved-gaseous $CH_4$ ($L_{MB}$, mM) | 140 | 144 | 142 | 138 | 159 | 161 | 138 |
| Equilibrium concentration for dissolved-hydrate $CH_4$ ($L_{GH}$, mM) | 64 | 64 | 64 | 64 | 63 | 63 | 64 |
| [POC] at sediment surface (wt %) | 0.42 | 0.42 | 0.42 | 0.68 | 0.68 | 0.68 | 0.37 |
| [$SO_4^{2-}$] at sediment surface (mM) | 29 | 26.5 | 27.5 | 28.4 | 26.8 | 24.5 | 32 |
| [$CH_4$] at sediment surface (mM) | 0 | 0 | 0 | 0 | 0 | 0 | 0 |
| [$I^-$] at sediment surface (μM) | 0.4 | 0.4 | 0.4 | 0.4 | 0.4 | 0.4 | 0.4 |

Belemnite (VPDB). The carbonatite NBS18 and limestone NBS19 were used as calibration standards. The $\delta^{13}C$ versus VPDB of NBS18 is −5.04‰ and NBS19 is +1.95‰. The precision of repeated analyses ($1\sigma$) was ± 0.5‰ [*Sun et al*., 2010].

## 4.2. Pore Water Analysis

[15] Sediment pore fluids were extracted onboard by centrifugation and filtering (0.45 μm) and then preserved at 4°C until laboratory analysis within a few weeks. For the analysis of ORI cores, sulfate ($SO_4^{2-}$), chloride ($Cl^-$), and iodide ($I^-$) concentrations were analyzed using ion chromatography with an analytical precision <5%. For the analysis of MD cores, pore water sulfate and chloride concentrations were measured using a Dionex ion chromatograph (model 4500i) equipped with a suppressed conductivity detector (Dionex, model CDM-2) and an IonPac AS4A anion exchange column (Dionex) [*Lim et al*., 2011]. A mixed solution of 1.7 mM $NaHCO_3$ (Merck) and 1.8 mM $Na_2CO_3$ (Merck) was used as the eluant and 0.025 N $H_2SO_4$ (Merck) as the regeneration fluid. Pore water samples were usually diluted 4000-fold with deionized water (Milli-Q) prior to analysis.

[16] The extracted pore fluids for iodide analysis were diluted by subboiling 0.3 N $HNO_3$ to reduce potential matrix artifacts during measurement. International Association for the Physical Sciences of the Oceans (IAPSO) and North Atlantic Surface seawater (NASS)-5 standards, as well as high purity multielements standard solutions, were used for calibration. Total dissolved iodide measurements were carried out using low-resolution inductively coupled plasma - mass spectrometry (ICP-MS). Procedural blanks were monitored every five analyses and the IAPSO standard solution was determined every 10 measurements to monitor instrumental stability and drift. The analytical precision for iodide was mostly better than 3%.

## 4.3. Other Determinations

[17] Porosity was determined by weight difference after freeze drying a known weight of wet sediment using a seawater density of 1.033 g $cm^{-3}$ and a dry sediment density of 2.5 g $cm^{-3}$, assuming that the pore space was completely filled with pore water.

[18] Sediment samples were dried at 60°C and weighed prior to determination of total carbon content. Following addition of 2 N HCl to remove inorganic carbonates and drying (60°C), POC content was determined in the ORI cores using an elemental analyzer (EA1110, ThermoQuest) with an analytical error of 0.02% for total organic carbon. For the MD cores, the instrument used was a Thermo Electron analyzer (model Flash EA 1112) equipped with a high-temperature resistance furnace and a TCD [*Lim et al*., 2011]. To obtain sedimentation rates of studied area, the chronology of two short piston cores, ORI-697-G21 (3.49 m in length; Yung-An Ridge) and ORI-697-G3 (3.08 m

in length; Good Weather Ridge), was investigated using $^{14}C$ dating on planktonic foraminifera. More than 200 specimens of *Neogloboquadrina dutertrei* (>250 m in size) were picked from the core bottoms and treated with $CH_3OH$ and NaOCl to remove contamination and organic matter on the foraminiferal shells. The specimens were then dated with an accelerator mass spectrometer at the Rafter Radiocarbon Laboratory, New Zealand.

[19] All analytical data are tabulated in the supporting information (Ts01, Ts02, Ts03, and Ts04).[1]

## 5. Numerical Modeling

[20] The following equations were solved to quantify the rates of reaction and transport of four dissolved ($I^-$, $CH_4$, $SO_4^{2-}$, DIC), and one solid (POC) species in the upper 30 m of sediments on the three ridges [*Berner*, 1980; *Boudreau*, 1997; *Haeckel et al*., 2004; *Wallmann et al*., 2006a]:

$$\Phi \cdot \frac{\partial C}{\partial t} = \frac{\partial\left(\Phi \cdot D_s \cdot \frac{\partial C}{\partial x}\right)}{\partial x} - \frac{\partial(\Phi \cdot v \cdot C)}{\partial x} + \Phi \cdot R_c + \Phi \cdot R_i \quad (1)$$

$$(1-\Phi) \cdot \frac{\partial G}{\partial t} = -\frac{\partial((1-\Phi) \cdot w \cdot G)}{\partial x} + (1-\Phi) \cdot R_c \quad (2)$$

where $x$ (cm) is sediment depth, $t$ (yr) is time, $\Phi$ is porosity, $D_s$ ($cm^2\ yr^{-1}$) is the solute-specific diffusion coefficient in the sediment, $C$ is the concentration of solutes in the pore water, $G$ is the POC content in dry sediment, $v$ ($cm\ yr^{-1}$) is the burial velocity of pore water, $w$ ($cm\ yr^{-1}$) is the burial velocity of solids, $R_C$ is the sum of reactions, and $R_i$ is the mixing rate due to bubble irrigation. Solutes were simulated in $mol\ L^{-1}$ of pore water (M) and POC in dry weight percent (wt %). Table 2 lists the physical parameter values used in the model.

[21] Sediment porosity decreases with depth due to steady-state compaction:

$$\Phi = \Phi_f + (\Phi_0 - \Phi_f) \cdot e^{-px} \quad (3)$$

where $\Phi_f$ is porosity below the depth of compaction, $\Phi_0$ is porosity at the sediment surface, and $p$ ($cm^{-1}$) is the depth attenuation coefficient of porosity. These parameters were determined from the measured porosity data at each site.

[1]Additional supporting information may be found in the online version of this article.

[22] Under the assumption of steady-state compaction, the velocity of interstitial fluids and solids is always directed downward. These were calculated as

$$v = \frac{\Phi_f \cdot w_f}{\Phi} \quad (4)$$

$$w = \frac{(1-\Phi_f) \cdot w_f}{(1-\Phi)} \quad (5)$$

where $w_f$ ($cm\ yr^{-1}$) is the burial velocity of compacted sediments calculated to be between 0.04 and 0.08 $cm\ yr^{-1}$ from the $^{14}C$ dating. As a first approximation, the same value of $w_f$ was imposed for Tai-Nan Ridge and Yung-An Ridge (0.04 $cm\ yr^{-1}$) and Good Weather Ridge (0.08 $cm\ yr^{-1}$). Sensitivity experiments show that our conclusions are insensitive to the choice of $w_f$ used in the model (see section 7). There were no geochemical indications of upward pore water advection resulting from deep dewatering processes.

[23] The sediment diffusion coefficient of each solute ($D_s$) was calculated according to Archie's law considering the effect of tortuosity on diffusion [*Boudreau*, 1997]:

$$D_s = \Phi^2 \cdot D_M \quad (6)$$

where $D_M$ ($cm^2\ yr^{-1}$) is the molecular diffusion coefficient at the in situ temperature, salinity, and pressure (Table 2) calculated according to *Boudreau* [1997].

[24] In this study, we consider irrigation of pore water in the upper 1–3 m of sediment due to rising gas bubbles. As bubbles ascend through tube structures, they create enhanced diffusion that mixes pore water in the sediment with seawater; similar to bioirrigation but extending over much greater depths [*Haeckel et al*., 2007]. The rate of irrigation of pore water due to gas bubble rise ($R_i$) was expressed as

$$R_i = \alpha_0 \cdot \frac{\exp\left(\frac{L_{irr}-x}{\alpha_1}\right)}{1+\exp\left(\frac{L_{irr}-x}{\alpha_1}\right)} \cdot (C_0 - C_i) \quad (7)$$

where $C_0$ is the solute concentration at the sediment surface, $\alpha_0$ ($yr^{-1}$) and $L_{irr}$ (cm) are two adjustable parameters that control the intensity and depth of bubble irrigation, respectively, and $\alpha_1$ (cm) determines how quickly bubble irrigation is attenuated to zero at the approximate depth of $L_{irr}$. The idea of using near-constant rates of

**Table 3.** Kinetic Rate Expressions Used in the Model

| Rate | Kinetic Rate Law[a] |
|---|---|
| Methane dissolution ($R_{MB}$) | $k_{MB} \cdot (L_{MB} - C_{CH_4})$ |
| Sulfate reduction ($R_{SR}$, mmol $cm^{-3}$ $yr^{-1}$ of $SO_4^{2-}$) | $0.5 \cdot f \cdot f_{SO_4} \cdot R_{POC}$ |
| Methanogenesis ($R_M$, mmol $cm^{-3}$ $yr^{-1}$ of $CH_4$) | $0.5 \cdot f \cdot (1 - f_{SO_4}) \cdot R_{POC}$ |
| Anaerobic oxidation of methane ($R_{AOM}$, mmol $cm^{-3}$ $yr^{-1}$ of $CH_4$) | $k_{AOM} \cdot C(SO_4) \cdot C(CH_4)$ |

[a] $R_{POC}$ is defined in equation (10), $k_{MB}$ is the kinetic constant of methane gas bubble dissolution (in $yr^{-1}$), $K_{SO_4}$ is the Michaelis-Menten kinetic constant for sulfate reduction (in mM), $k_{AOM}$ is the rate constant for AOM (in $mmol^{-1}$ $cm^3$ $yr^{-1}$), and $f_{SO4} = SO_4^{2-}/(SO_4^{2-} + K_{SO_4})$, the Michaelis-Menten rate-limiting term for sulfate reduction. The factor, $f = (d_s \times (1 - \Phi) \times 10)/(MW_C \times \Phi)$ is used to convert between solid and dissolved carbon, where $MW_C$ is the molecular weight of carbon (12 g $mol^{-1}$) and $d_s$ is the density of dry solids (2.5 g $cm^{-3}$). Other symbols are described in the text.

irrigation down to a depth $L_{irr}$ is based on simulations of sediments affected by $CH_4$ gas venting in the Sea of Okhotsk [*Haeckel et al*., 2007]. Although a mechanistic theory that explains this phenomenon has not been reported, the gas bubbles may manage to form their own small fractures and tubes in the muddy, unconsolidated near-surface sediments [*Algar et al*., 2011]. Once these high-permeability conduits are formed, rising bubbles are able to reach a terminal rise velocity and, subsequently, are released rapidly from the sediment to the water column [*Haeckel et al*., 2007]. Although this process was not observed directly, there is evidence to suggest that it is an important pathway for transporting methane into the upper 30 m of sediment at all study sites (see section 7) as well driving mixing between pore water and seawater in the upper few meters (see section 6).

[25] In this paper, we focus on the major sinks for methane, sulfate, and POC in anoxic marine sediments (Table 3). The cycles of nitrogen, manganese, and iron are considered to be unimportant for sulfate and methane cycling in these settings [cf. *Holmkvist et al*., 2011]. Sulfate is the major electron acceptor for microbial degradation of POC in anoxic marine sediments [*Westrich and Berner*, 1984; *Jørgensen and Kasten*, 2006; *Thullner et al*., 2009]. The mineralization of POC during sulfate reduction can be expressed as

$$2(CH_2O)(I^- r_I) + SO_4^{2-} \rightarrow 2HCO_3^- + H_2S + 2r_I I^- \quad (8)$$

where $CH_2O$ is the nominal stoichiometry of POC (oxidation state = 0). Iodide ($I^-$) is released from the organic matter concomitant with inorganic carbon with an atomic iodine to carbon ratio, $r_I$, determined from the $I^-$ data. No phosphate or ammonium data is available to constrain the regeneration ratios of these compounds.

[26] Reactive POC buried below the sulfate reduction zone is degraded biogenically by methanogenic organisms:

$$2(CH_2O)(I^- r_I) \rightarrow CO_2 + CH_4 + 2r_I I^- \quad (9)$$

[27] The rates of sulfate reduction and methanogenesis are defined according to the kinetic expressions in Table 3, and depend on the the total rate of POC degradation, $R_{POC}$.

[28] The calculation of RPOC, follows the rate law proposed by *Middelburg* [1989] and later modified by *Wallmann et al*. [2006a]:

$$R_{POC} = \frac{K_C}{C(DIC) + C(CH_4) + K_C} \cdot \left(0.16 \cdot \left(a_0 + \frac{x}{w}\right)^{-0.95}\right) \cdot POC \quad (10)$$

where $K_C$ (M) is an inhibition coefficient for POC degradation, $C(DIC)$ and $C(CH_4)$ are the simulated concentrations of dissolved inorganic carbon (DIC) and methane, respectively, and $a_0$ (yr) is the initial age of organic matter, which reflects the age of the organic matter buried below the bioturbated surface layer [*Middelburg*, 1989]. The parameterization of POC degradation was achieved using values that were either determined in this study by inverse modeling of the measured data or taken from *Wallmann et al*. [2006a]. Due to a lack of DIC data, simulated DIC concentrations were used to determine POC degradation rates. The net reaction terms ($R_C$ in equation (1)) of $I^-$, $CH_4$, $SO_4^{2-}$, and POC are given in Table 4.

[29] Methane produced at depth can ascend toward the sulfate reduction zone where it can be consumed by AOM [*Barnes and Goldberg*, 1976]:

$$CH_4 + SO_4^{2-} \rightarrow HCO_3^- + HS^- + H_2O \quad (11)$$

[30] The rate of AOM ($R_{AOM}$) was simulated using bimolecular kinetics [*Regnier et al*., 2011] (Table 3).

[31] Gaseous methane was not explicitly included in the model. However, dissolution of the gas bubbles rising through the sediment was considered:

$$CH_{4(g)} \rightarrow CH_4 \quad \text{if } CH_4 \leq L_{MB} \quad (12)$$

where $L_{MB}$ (M) is the in situ methane gas solubility concentration [*Haeckel et al*., 2004] calculated

**Table 4.** Reaction Terms Used in the Model ($R_C$, Equation (1)).

| Species | Rates |
|---|---|
| Particulate organic carbon (POC) | $-R_{POC}$ |
| Sulfate ($SO_4^{2-}$) | $-R_{SR}-R_{AOM}$ |
| Methane ($CH_4$) | $+R_M-R_{AOM}+R_{MB}$ |
| Iodide ($I^-$) | $+r_I R_{POC}$ |

using the algorithm of *Duan et al*. [1992a, [1992b] and the site-specific salinity, temperature, and pressure at the seafloor. The rate of gas dissolution ($R_{MB}$) depends on the difference between $L_{MB}$ and the in situ methane concentration using a first-order rate constant $k_{MB}$ ($yr^{-1}$) (Table 3). The $k_{MB}$ value is a fitting parameter that accounts for the rate of gas dissolution in addition to diffusion of dissolved gas through the bubble tubes and walls.

[32] Upper boundary conditions were set to values measured at or near the sediment-water interface. Fixed concentrations were imposed for solutes and POC. The upper boundary DIC, $SO_4^{2-}$, and $I^-$ concentrations were set to seawater values. Zero concentration gradients (Neumann type) were imposed for all solutes at the lower boundary. The method-of-lines was used to transfer the set of finite difference equations of the spatial derivatives of the coupled partial differential equations to the ordinary differential equation solver (NDSolve) in MATHEMATICA v. 7.0. All models were run for $4\times10^5$ years to achieve steady state using a grid spacing which increased from ~2 cm at the sediment surface to 57 cm at depth. Mass conservation was typically better than 99.5%.

## 6. Results

### 6.1. Geochemistry

[33] Geochemical data from each ridge are shown in Figure 2. Methane was the dominant hydrocarbon gas at all sites with maximum concentrations of 2.14 mM below the SMT on Yung-An Ridge (Figure 2a). These are minimum values because of degassing artifacts during core retrieval [*Paull et al*., 2000], observable by the scatter in the data below the SMT and decrease in methane to concentrations approaching the solubility at atmospheric pressure. Ethane was detected in cores MD05-2911 (0.1–1.16 μM) and MD05-2913 (0.34–0.56 μM) but higher hydrocarbons were below detection limit (supporting information). Methane concentrations diminished sharply at the SMT due to AOM, which explains the absence of methane above this depth [*Schulz et al*., 1994]. The depth of the SMT varied among the three ridges with no clear trend, which mainly reflects variability in the reactivity of POC and the upward flux of methane from deeper sediment layers (see below).

[34] Sulfate concentrations deviated from the expected linear decrease from the surface down to the SMT observed in continental margin sediments [*Borowski et al*., 1996]. Sulfate decreased only slightly from seawater values between the sediment surface and 1–3 mbsf at all sites (Figure 2b). This is clearly seen by the red lines in Figure 2b that show the theoretical linear sulfate profiles if AOM in the SMT were the only sink for sulfate diffusing into the sediment from the seawater with negligible influence from sediment compaction. Below this depth, sulfate concentrations decreased nearly linearly down to the SMT. Iodide concentrations (Figure 2c) also showed little variation in the upper 3 m and then increased due to microbial degradation of POC. This was also true for Good Weather Ridge, although low data resolution did not reveal the same trend for sulfate.

[35] The highest iodide concentrations (0.317 mM) were obtained on Yung-An Ridge (Figure 2c), although the sharp concentration gradients in all cores suggest that POC mineralization extended beyond the depth of the retrieved cores on Tai-Nan Ridge. It is interesting to note that the slopes of the sulfate and iodide profiles below the irrigated surface layer on Tai-Nan Ridge were less steep in core MD05-2912 than ORI-860-1 and ORI-860-2. Additionally, the iodide data in MD05-2912 revealed relatively lower values (<0.2 mM) than the other two MD cores, which may result from low POC degradation rates. In support of this idea, POC data showed no clear decrease with depth on Tai-Nan Ridge in core MD05-2912 compared to core MD05-2911 on Yung-An Ridge (Figure 2d).

[36] Chloride concentrations showed variable trends (Figure 2e). At Site MD05-2911 on Yung-An Ridge, chloride increased to 622 mM below 20 mbsf, which could indicate hydrate formation [*Haeckel et al*., 2004]. For comparison, the chloride pore water concentration at a reference site on Tai-Nan Ridge was ~562 mM (see supporting information). Good Weather Ridge displayed the opposite trend, with chloride decreasing sharply from 546 mM at 809 cm below the seafloor (cmbsf) to 505 mM at 1109 cmbsf, possibly due to dissociation of gas hydrates [*Hesse and Harrison*, 1981].

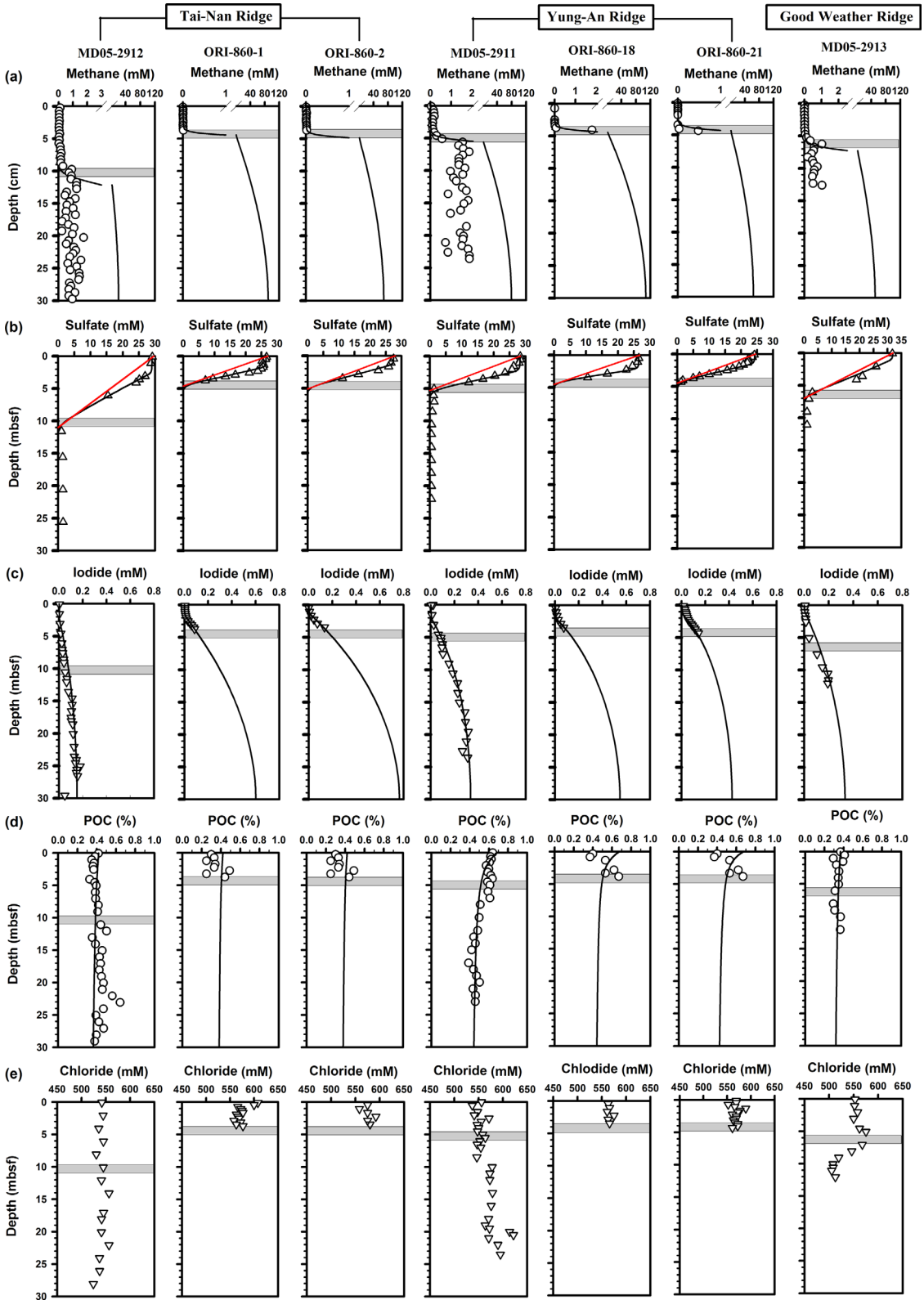


**Figure 2.** Depth profiles of measured (symbols) and modeled (curves) concentrations of (a) dissolved methane, (b) sulfate, (c) iodide, (d) POC, (e) chloride, and (f) porosity data. POC data from the ORI sites were not available, and data from the proximate Site ORI-697 are shown for ORI-860-1 and ORI-860-2 and data from ORI-718 are shown for ORI-860-18 and ORI-860-21. SMT depths are represented by the horizontal gray bars. Red lines in Figure 2b represent the theoretical linear sulfate profiles if AOM in the SMT were the only sink for sulfate diffusing into the sediment from the seawater.

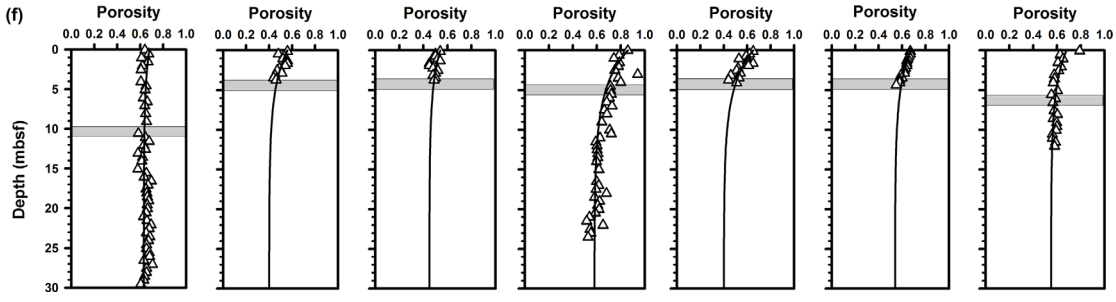


**Figure 2.** Continued.

[37] Headspace $\delta^{13}$C-$CH_4$ ranged from ~ −54.4‰ to −95.0‰ across the ridges (Figure 3). Together with $C_1/C_2$ ratios (see supporting information), the gas origin was consistent with microbial sources (−50‰ to −110‰, $C_1/(C_2+C_3)>10^3$) [*Whiticar*, 1999]. The lowest $\delta^{13}$C-$CH_4$ values were observed at the SMT depth on all ridges (−82.5 to −95.0‰). $CH_4$ became progressively enriched in $^{13}$C on Tai-Nan Ridge from the SMT down through the methanogenic zone to a maximum of −57‰ at ~29.5–30 mbsf. On Tai-Nan Ridge, $\delta^{13}$C-$CO_2$ increased from −27.4‰ below the SMT to −15.7‰ near the surface, presumably due to mixing of seawater ($\delta^{13}$C-$CO_2$ = 0‰) with $CO_2$ released from mineralized phytodetritus [$\delta^{13}$C-$CO_2 \approx$ −20‰; *Meyers*, 1994].

## 6.2. Transport-Reaction Modeling

[38] Model simulations for the three ridges showed a good correspondence with the field data (Figure 2) with the exception of methane. As mentioned previously, the measured methane concentrations were affected by degassing during core recovery, whereas the model predicts the theoretical in situ methane concentrations.

[39] Model-derived parameters values are presented in Table 5 along with details on how they were constrained by inverse modeling of the data. The data were simulated using the same values of the constant that inhibits POC mineralization ($K_C$ = 40 mM), the kinetic constant for AOM ($k_{AOM}$ = 20 $yr^{-1}$ $M^{-1}$), the Michaelis-Menten constant for sulfate reduction ($K_{SO_4}$ = 0.1 mM) and the irrigation parameters $\alpha_0$ and $\alpha_1$ at all sites. These values are of the same order of magnitude ($k_{AOM}$ = 1–20 $yr^{-1}$ $M^{-1}$; $K_C$ = 30–40 mM; $K_{SO_4}$ = 1.0 mM) as those derived by *Wallmann et al.* [2006a]. The parameter $k_{AOM}$ controls the sharpness of the overlap between the sulfate and methane profiles and the value implemented in the

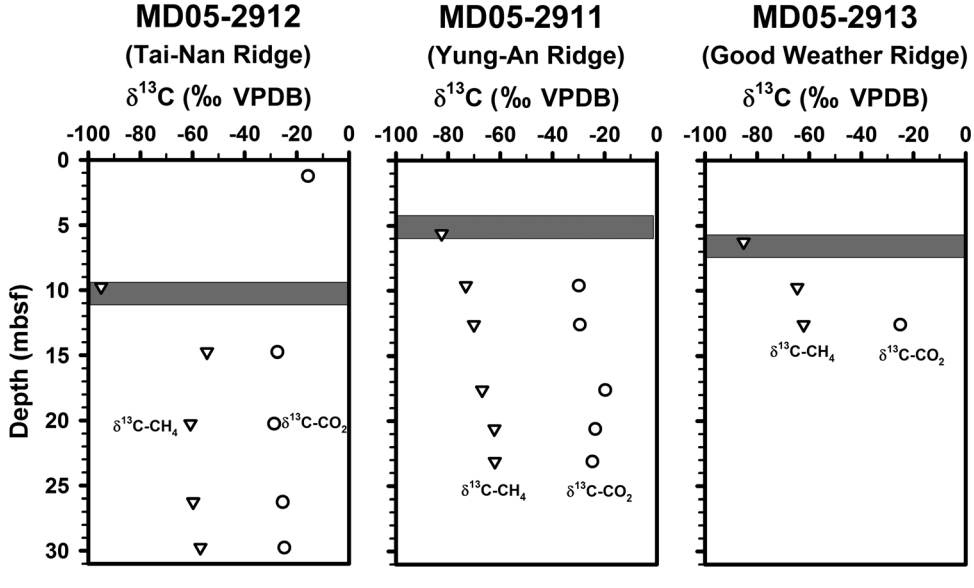


**Figure 3.** Depth profiles of headspace carbon isotope compositions for methane ($CH_4$) and carbon dioxide ($CO_2$). SMT depths are represented by gray bars.

**Table 5.** Derived Parameter Values at Each Site/Ridge

| | Tai-Nan | | | Yung-An | | | Good Weather |
|---|---|---|---|---|---|---|---|
| Parameter[a] | MD05-2912 | ORI-860-1 | ORI-860-2 | MD05-2911 | ORI-860-18 | ORI-860-21 | MD05-2913 |
| POC inhibition constant ($K_C$, mM) | 40 | 40 | 40 | 40 | 40 | 40 | 40 |
| Kinetic constant for AOM ($k_{AOM}$, $yr^{-1}$ $M^{-1}$) | 20 | 20 | 20 | 20 | 20 | 20 | 20 |
| Michaelis-Menten constant for sulfate reduction ($K_{SO_4}$, mM) | 0.1 | 0.1 | 0.1 | 0.1 | 0.1 | 0.1 | 0.1 |
| Atomic I/C ratio for organic matter degradation ($r_I$, mol $I^-$/mol C) | $1.2\times10^{-2}$ | $1.7\times10^{-2}$ | $2.5\times10^{-2}$ | $1.3\times10^{-2}$ | $8\times10^{-3}$ | $1.05\times10^{-2}$ | $1.2\times10^{-2}$ |
| Initial age of POC ($a_0$, kyr) | 50 | 50 | 50 | 2 | 2 | 2 | 16.5 |
| Bubble irrigation parameter ($L_{irr}$, cm) | 280 | 180 | 150 | 250 | 230 | 150 | 120 |
| Kinetic constant for methane gas dissolution ($k_{MB}$, $yr^{-1}$) | $1.1\times10^{-5}$ | $2.8\times10^{-5}$ | $2.0\times10^{-5}$ | $4.5\times10^{-5}$ | $3.0\times10^{-5}$ | $1.7\times10^{-5}$ | $2.5\times10^{-5}$ |
| Irrigation coefficient ($\alpha_0$, $yr^{-1}$) | 0.1 | 0.1 | 0.1 | 0.1 | 0.1 | 0.1 | 0.1 |
| Irrigation coefficient ($\alpha_1$, cm) | 5 | 5 | 5 | 5 | 5 | 5 | 5 |

[a] $K_c$, $k_{AOM}$, $K_{SO_4}$ were based on values reported by Wallmann *et al*. [2006a]. $r_I$ was determined using the measured iodide profile. The $a_0$ value was constrained from the measured POC data in the MD cores only. $L_{irr}$ was determined from the depth in the sulfate and iodide data in the upper few meters of sediment where the largest change in concentration occur. The $\alpha_1$ value was constrained from the curvature of the sulfate and iodide profiles at this depth. The $k_{MB}$ value was constrained from the depth of the SMT. The $\alpha_0$ value affects the simulation of the entire sulfate and iodide profiles and was constrained from the concentration data in addition to the depth of the SMT.

model provides an adequate fit to the data. The atomic I/C ratios of in the organic material ($8\times10^{-3}$ – $2.5\times10^{-2}$) varied among sites and were also similar ($r_I = 1.2\times10^{-3}$ – $1.0\times10^{-2}$) to those obtained by *Wallmann et al*. [2006a] for slope sediments but 2 orders of magnitude larger than those reported by *Lu et al*. [2008] for Cascadia Margin ($r_I = 3.0\times10^{-4}$). It is presently unclear whether this reflects preferential mineralization of iodide or higher particulate organically bound iodine concentrations at our study sites.

[40] The parameters that differed among the three ridges are the initial age of POC ($a_0$), the depth of bubble irrigation ($L_{irr}$) and the kinetic constant of methane gas dissolution ($k_{MB}$). Due to a lack of deep POC data in the ORI cores, $a_0$ values were constrained from the POC data from the MD cores and assumed to be invariant for each ridge, whereas $k_{MB}$ and $L_{irr}$ were site-specific (Table 5). Although this introduces a level of uncertainty to the results, the sensitivity analysis and budget developed below show that any error introduced into the sulfate and methane budget by assuming constant initial ages for each ridge is likely to be small.

[41] Table 6 lists the calculated depth-integrated turnover rates and fluxes for the individual modeled cores as well as the averages for each ridge. In all cases, the highest and lowest depth-integrated reaction rates were associated with Yung-An and Tai-Nan Ridge, respectively, with Good Weather Ridge displaying intermediate values. The mean total depth-integrated rate of POC mineralization was 5 times higher on Yung-An Ridge (102 mmol $m^{-2}$ $yr^{-1}$) than on Tai-Nan Ridge (19 mmol $m^{-2}$ $yr^{-1}$). However, mean depth-integrated sulfate reduction rates on Yung-An Ridge (39 mmol $m^{-2}$ $yr^{-1}$) were a factor of 8 higher than those on Tai-Nan Ridge (4.7 mmol $m^{-2}$ $yr^{-1}$), and four times as high as those on Good Weather Ridge (9.5 mmol $m^{-2}$ $yr^{-1}$). These differences exemplify the presence of labile POC degraded in the sulfate reduction zone on Yung-An Ridge. Here, the initial age of POC ($a_0$) was 2 kyr, compared to 50 kyr for Tai-Nan Ridge (Table 5).

[42] Depth-integrated methanogenesis rates were less variable between the ridges, varying from only 5 to 13 mmol $m^{-2}$ $yr^{-1}$. Dissolution of externally supplied gas provided 4 to 6 times as much methane as methanogenesis, with depth-integrated rates of up to 53 mmol $m^{-2}$ $yr^{-1}$ on Yung-An Ridge and 31 mmol $m^{-2}$ $yr^{-1}$ on Tai-Nan Ridge. The methane concentrations above the SMT were not visibly increased by the dissolution of bubbles because of rapid methane consumption by AOM. Recent evidence also suggests that methane may be rapidly consumed on the walls of sediment fractures and tubes by methanotrophic microbial biofilms [*Briggs et al*., 2011].

[43] The fraction of POC buried varied from 62 to 90% (Table 6). These values are higher than carbon burial efficiencies of 1 to 50% for continental margin sediments [*Burdige*, 2007], since only sulfate reduction and methanogenesis were considered. Aerobic respiration may consume up to 50% of deposited carbon [*Jørgensen and Kasten*,

**Table 6.** Depth-Integrated Turnover Rates (mmol $m^{-2}$ $yr^{-1}$) and Fraction of POC Buried (%) for Offshore SW Taiwan

| | Tai-Nan | | | | Yung-An | | | | Good Weather |
|---|---|---|---|---|---|---|---|---|---|
| | MD05-2912 | ORI-860-1 | ORI-860-2 | Average | MD05-2911 | ORI-860-18 | ORI-860-21 | Average | MD05-2913 |
| $F_{SR}$: Sulfate reduction via POC degradation (mmol $m^{-2}$ $yr^{-1}$ of $SO_4^{2-}$) | 5.6 | 4.2 | 4.3 | 4.7 | 32 | 47 | 37 | 39 | 9.5 |
| $F_M$: Methane formation via POC degradation (mmol $m^{-2}$ $yr^{-1}$ of $CH_4$) | 3.3 | 5.8 | 5.6 | 4.9 | 11 | 15 | 13 | 13 | 8.6 |
| Total POC mineralization rate (mmol $m^{-2}$ $yr^{-1}$ of C) | 17 | 20 | 20 | 19 | 83 | 121 | 99 | 102 | 35 |
| POC deposition rate (mmol $m^{-2}$ $yr^{-1}$ of C) | 129 | 210 | 193 | 177 | 238 | 340 | 261 | 280 | 275 |
| $F_B$: POC burial rate (mmol $m^{-2}$ $yr^{-1}$ of C) | 112 | 190 | 173 | 158 | 155 | 219 | 162 | 178 | 240 |
| Fraction of POC buried (%)[a] | 87 | 90 | 90 | 89 | 65 | 64 | 62 | 64 | 87 |
| $F_{AOM}$: Anaerobic oxidation of methane (mmol $m^{-2}$ $yr^{-1}$ of $CH_4$)[b] | 25 | 25 | 22 | 24 | 71 | 37 | 35 | 48 | 34 |
| $F_{MB}$: Gas dissolution (mmol $m^{-2}$ $yr^{-1}$ of $CH_4$) | 28 | 35 | 29 | 31 | 82 | 40 | 36 | 53 | 49 |
| Benthic flux of $SO_4^{2-}$ (mmol $m^{-2}$ $yr^{-1}$ of $SO_4^{2-}$) | 31 | 29 | 26 | 29 | 104 | 84 | 72 | 87 | 44 |
| Methane flux emitted to water column (mmol $m^{-2}$ $yr^{-1}$ of $CH_4$) | 0.6 | 0.9 | 0.5 | 0.7 | 2.7 | 1.5 | 0.7 | 1.6 | 0.7 |
| Methane flux buried to deep sediments (>30 m) (mmol $m^{-2}$ $yr^{-1}$ of $CH_4$) | 5.2 | 14 | 12 | 10 | 18 | 17 | 14 | 16 | 22 |

[a]Calculated as $F_B/(2\times(F_{SR}+F_M)+F_B)$.
[b]Note that AOM rates are lower than gas dissolution rates ($F_{MB}$) because a significant fraction of dissolved methane is buried with the accumulating sediment ($F_B$).

2006]. Thus, the POC dynamics across the ridges studied here are broadly representative of continental margin sediments.

[44] At all sites, the bulk of the methane was oxidized anaerobically by AOM with depth-integrated rates increasing from 24 mmol $m^{-2}$ $yr^{-1}$ on Tai-Nan Ridge to 48 mmol $m^{-2}$ $yr^{-1}$ on Yung-An Ridge. AOM was by far the largest sink for sulfate on Tai-Nan and Good Weather ridges, consuming ~4–5 times as much sulfate as POC mineralization. On Yung-An Ridge, depth-integrated AOM and sulfate reduction rates were more comparable. The derived depth-integrated AOM rates were similar to sites studied in the Black Sea, Skagerrak, Sea of Okhotsk, and the Namibian shelf where upward fluid flow is absent [*Fossing et al*., 2000; *Jørgensen and Nelson*, 2004; *Wallmann et al*., 2006a; *Dale et al*., 2008]. Yet, the depth-integrated rates are orders of magnitude lower than sediments at sites with upward fluid flow [*Albert et al*., 1998; *Wallmann et al*., 2006b]. A significant fraction (24 to 38%) of dissolved methane was buried with the pore water, and a small fraction (<2%) was lost to the overlying water (Table 6). However, the model does not account for aerobic oxidation pathways, which would consume dissolved methane at the sediment-water interface. More importantly, the flux of methane that is lost directly from the sediment in the rising bubbles cannot be quantified with the current model, and this flux likely outweighs any loss of dissolved methane to the water column [*Alperin and Hoehler*, 2009]. Future studies are needed to address the gas bubble flux on the upper slope and the passive continental margin in order to derive a regional methane budget.

## 7. Discussion

### 7.1. Bubble Irrigation as a Methane Supply Pathway

[45] The sulfate profiles measured in all cores are concave-up, that is, they deviate below the red lines in Figure 2b, indicating a source of sulfate in the upper 1–3 m. Analogously, iodide concentrations varied little from seawater values over the same depth. These observations indicate that the distribution of sulfate and iodide in these upper sediment layers is controlled by the same process that acts to restore sediment concentrations toward seawater values.

[46] The similarity of sulfate and iodide concentrations in the upper 1–3 m to those in the bottom

water was attributed to a pseudoirrigation process driven by gas bubbles rising through escape tubes [*Haeckel et al*., 2007]. Similarly shaped solute profiles have been reported for passive [*Schulz et al*., 1994; *Niewöhner et al*., 1998; *Fossing et al*., 2000; *Zabel and Schulz*, 2001; *Hensen et al*., 2003] and active margin sediments [*Schmidt et al*., 2005; *Haeckel et al*., 2007; *Coffin et al*., 2008; *Feseker et al*., 2010; *Schwalenberg et al*., 2010; *Tryon et al*., 2010]. Irrigation driven by gas bubbles rising through open bubble tubes or vacant animal burrows was proposed by *Martens* [1976] and the theory developed further by *Haeckel et al*. [2007]. The idea is based on enhanced diffusive mixing in the wake of rising bubbles, leading to a homogenization of concentration gradients between the sediment and the overlying seawater. The study by *Schwalenberg et al*. [2010] on the Hikurangi Margin nicely illustrates how the impact of bubble irrigation on solute concentrations decreases in intensity with increasing distance from a gas chimney. The different values of the parameters $L_{irr}$ and $k_{MB}$ derived in this study could therefore reflect the proximity of coring to the gas vents. Other possibilities that could be argued to produce similar profiles include bioirrigation, inhibition of sulfate reduction, and nonsteady state effects. In the following paragraphs, we shall address each of these cases individually.

[47] The potential role of meter-scale bioirrigation (pumping of seawater through animal burrows) was first addressed by *Fossing et al*. [2000] in sediments from the SE Atlantic lying at 2000 m water depth. These authors observed tubes structures >3 m depth with fecel pellets inside of it but did not find any organism living within the tubes. They speculated that gas ebullition could also produce similar profiles, but evidence to support this idea was lacking. No animals were observed in our cores below the upper few centimeter of sediment. On this basis alone, we reject the presence of animal deep with the sediment as a viable mechanism to explain our data.

[48] Per mole of carbon oxidized, aerobic respiration, denitrification, and dissimilatory iron reduction yield more usable energy to the heterotrophic microbial community compared to sulfate reduction [e.g., *Jørgensen and Kasten*, 2006]. High concentrations of $O_2$, $NO_3^-$, and reactive $Fe^{III}$ in the surface sediments would inhibit microbial sulfate reduction, leading to sulfate concentration profiles that vary little from the bottom water value with depth. Only when $O_2$, $NO_3^-$, and $Fe^{III}$ are diminished to very low levels will sulfate reduction become the most favorable carbon oxidation pathway. Our applied model does not consider $O_2$, $NO_3^-$, and $Fe^{III}$, since they are normally consumed within a few centimeters of the sediment surface in continental margin sediments and have little effect on meter-scale sulfate and methane dynamics. Only in highly oligotrophic settings characterized by little reactive organic carbon, such as deep-sea sediments, does sulfate reduction play a minor role in carbon mineralization. Exploratory model simulations (not shown) indeed show that when bubble irrigation is turned off, the sulfate profiles in Figure 2b cannot be reproduced with the explicit consideration of aerobic respiration, denitrification, and dissimilatory iron reduction. In any case, inclusion of these processes would have no bearing on the iodide profiles, which also show the characteristic irrigation-like features. These arguments rule out inhibition of sulfate reduction by other electron acceptors as an explanation of the sulfate and iodide trends in the upper meters.

[49] Deposition of a 2–3 m thick sediment layer following gravity-driven sedimentary slides could also produce the sulfate and iodide profiles observed here [*Hensen et al*., 2003; *Henkel et al*., 2011]. The idea is that during a turbidite event, mud is mixed with seawater as it moves downslope, resulting in a freshly deposited mud layer with seawater sulfate (and iodide) concentrations in the resulting pore space. In the decades following the slide event, molecular diffusion would smooth out the sharp gradients in the resulting concentration profiles, leading to trends that look very similar to those in Figure 2 [*Hensen et al*., 2003]. However, this mechanism is unlikely in the cores studied, primarily because they were sampled on top of ridges rather than at the bottom of the continental slope [*Hensen et al*., 2003]. Nonetheless, settling of turbidites in local sites of minimal potential energy cannot be ruled out. Yet, the nonsteady state effects invoked by *Henkel et al*. [2011] and *Hensen et al*. [2003] were based on several types of sedimentological evidence, such as abrupt changes in TOC content, grain size, and magnetic susceptibility. Four additional cores taken from the peaks and flanks of Yung-An Ridge reveal that the major constituent of these sediments is homogeneous mud in the upper 10 m with no obvious sorting by grain size induced by sediment transport in turbidites (Lin et al., unpublished data). In addition, one may expect to see erosional contacts at the base of turbidtes marked by a distinct peak in magnetic susceptibility [*Hensen et al*., 2003]. The magnetic susceptibility in our MD cores was very low and showed no such

peaks at the depth of the irrigated layer (Horng et al., unpublished data).

[50] It is also worth noting that these profiles also could not be produced by any reasonable change in the deposition rate of pelagic material. The transport of pore water in the upper 3 m is strongly dominated by molecular diffusion (Peclet number ($v \times 300$ cm $\times D_s^{-1}$) $<<$ 1 for all solutes). Hence, diffusion would rapidly dampen any effect of enhanced sulfate input due to increased accumulation of sediment at the sediment surface.

[51] In summary, we advance the idea of bubble irrigation as a key transport mechanism because (i) acoustic blanking in seismic profiles along the ridges, the BSR and observed gas plumes in the water column all convincingly illustrate that there is a large amount of gas in the sediments offshore SW Taiwan, (ii) no irrigating animals were observed in deep sediments in our cores, (iii) carbon oxidation by other electron acceptors has no effect on the sulfate profiles when bubble irrigation is turned off, and (iv) the role of turbidites can be discounted. As will be shown in the following analysis, a source of gaseous methane rising through the sediment is required to predict the correct depth of the SMT at all sites.

## 7.2. Relating Geochemistry to the Geological Setting

[52] Of the model parameters, only $a_0$, $L_{irr}$, $k_{MB}$, $r_I$, and $w_f$ varied between the ridges. Although these parameter values cannot be independently verified in this study, sensitivity tests show that they can be well constrained (Figure 4). Further simulations varying $L_{irr}$, $a_0$, $k_{MB}$, and $w_f$ were performed to determine the sensitivity of the sulfate, methane, and POC profiles to these parameters. ($r_I$ only affects iodide and is not relevant in this regard). Core MD05–2911 was used for this purpose since the most complete data set was available here, although similar results were obtained for all ridges (data not shown). The results show the effect of varying $L_{irr}$ by $\pm$ 50%, $a_0$ between 0.2 and 20 kyr, $k_{MB}$ between 0 and $4\times10^{-4}$ $yr^{-1}$, and $w_f$ between 0.01 and 0.08 cm/yr (Figure 4).

[53] The value of $a_0$ greatly affects the POC content as expected (Figure 4a), with larger ages leading to greater POC content. Similarly, POC content is affected by the changes of sedimentation rate ($w_f$), whereas sulfate and methane concentrations and the SMT depth show little variation (Figure 4b). However, this parameter has only a minor effect on sulfate and methane concentrations, demonstrating that AOM driven by methane supplied from depths >30 m is the strongest sink for sulfate and methane. $L_{irr}$ has a moderate effect on the depth of sulfate penetration and a minor effect on POC content (Figure 4c) by altering the DIC concentrations and hence the rate of POC mineralization (equation (10)). Sulfate and methane concentrations are most sensitive to $k_{MB}$ (Figure 4d). In the case of no-methane flux from gas dissolution ($k_{MB}$=0 $yr^{-1}$), sulfate penetrates to almost 20 mbsf and methane concentrations at depth diminish to a few millimolars. This illustrates that the methane used to consume sulfate must originate from sediments deeper than those recovered

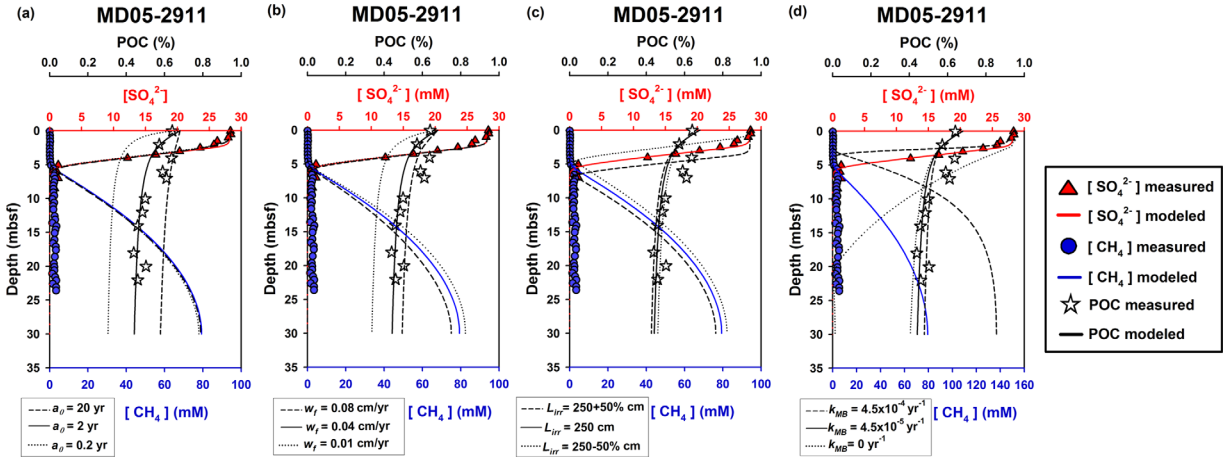


**Figure 4.** Sensitivity of sulfate, methane, and POC content at Site MD05–2911 (dashed and dotted curves) to the following parameters: (a) the initial age of POC ($a_0$), (b) the sedimentation rate ($w_f$), (c) the bubble irrigation depth ($L_{irr}$), and (d) the rate constant for methane bubble dissolution ($k_{MB}$). Solid curves denote the standard simulation results ($a_0$ = 2 kyr, $w_f$ =0.04 cm $yr^{-1}$, $L_{irr}$ = 250 cm, and $k_{MB}$ = $4.5\times10^{-5}$ $yr^{-1}$).

here with the coring devices. Externally supplied methane is required to sustain the SMT at the observed depth because the reactivity of the organic matter is simply too low to produce enough methane production within the upper 30 m. We argue that this provides further evidence for the role of ascending gas in producing the irrigation patterns in the solute profiles, rather than the alternatives discussed in the previous section.

[54] The $k_{MB}$ values displayed no obvious trend across the ridges (Table 5). This is because $k_{MB}$ was constrained from the SMT depth, which in turn is determined by the processes which add (irrigation) and remove (POC mineralization, AOM) sulfate from the sediment. For example, stations MD05–2911 and ORI-860-21 on Yung-An Ridge have similar SMT depths and depth-integrated rates of sulfate reduction (Table 6) but irrigation depths of 250 and 150 cm, respectively (Table 5). Because sulfate influx by irrigation is much greater at MD05–2911, more gas-derived methane must be dissolving into the sediment at this station to maintain the correct SMT depth. Hence, $k_{MB}$ is $4.5\times10^{-5}$ $yr^{-1}$ at MD05–2911 but only $1.7\times10^{-5}$ $yr^{-1}$ at ORI-860-21.

[55] Bulk POC degradation rates are not only inhibited by methane and DIC accumulations but also depend on the POC input flux, the sedimentation velocity ($w$), and the initial age ($a_0$) (equation (10)). The latter were determined from the downcore trends in POC data in the long MD cores where sufficient data were available to constrain the mineralization kinetics. The POC contents in the shorter ORI cores showed less obvious trends as those in the MD cores, and the application of the POC decay model to these sites is associated with uncertainties. The lowest $a_0$ (2 kyr) was derived for Yung-An Ridge, whereas for Tai-Nan Ridge an initial age of 50 kyr was required to simulate the data. Good Weather Ridge was characterized by intermediate values (16.5 kyr). These fall within the range reported for ODP sites off Costa Rica (Site 1041), Peru (685 and 1230), Chile (1233), California (1014), Namibia (1084), and the east coast of the United States (Blake Ridge, Site 995) [*Marquardt et al*., 2010].

[56] The value $a_0$ is dependent on the decomposition of POC during transit through the water column [*Middelburg*, 1989]. The transit time of exported POC to the seafloor is presumably similar at all sites investigated here, which fails to explain the high variability in $a_0$ observed in this study. *Wallmann et al*. [2006a] attributed high initial ages of POC ($a_0 = 30$ kyr) for the shelf of Sakhalin Island, Sea of Okhotsk, to loss of surface sediments during sampling due to overpenetration of the coring device. We cannot be sure that the same artifacts did not occur during our sampling. However, the curvature in the POC profile at Site MD05–2911 on Yung-An Ridge, indicating degradation of the reactive organic carbon components, extends over the upper 15 m of sediment (Figure 2d). It is not possible that 15 m of surface sediment was lost from the other ridges that display less curvature in the POC profiles. Thus, the different $a_0$ probably reflect past or present changes in sedimentation rates across the ridges. Nonetheless, this does not alter the fact that externally supplied methane is the major control on the variable sulfate and methane gradients across each ridge (Table 6).

[57] To summarize these findings, we propose that emergent thrusts on Yung-An Ridge provide conduits for free gas to be transported from below the BSR to the surface sediments. The variation of depth-integrated gas dissolution rates among the individual sampling sites on Yung-An Ridge probably reflects the proximity of the coring locations to the faults (Table 6). Site MD05–2911 is located on top of homoclines where fractures and normal faults develop. Consequently, acoustic turbidity occurs close to the sea floor (Figure 1c), and depth-integrated dissolution and AOM rates are higher here than at the neighboring coring locations which are located on the west limb of the homoclines. Similarly, at Good Weather Ridge where the sampling site was situated above a large area with free gas, the depth-integrated dissolution rates are comparable to Yung-An Ridge (Table 6). Even though Site MD05–2913 is on the opposite flank of the emergent trust of Good Weather Ridge, depth-integrated rates are higher than sites on Tai-Nan Ridge. Compared to the other two ridges, the blind fault underneath Tai-Nan Ridge and the anticline which serves as a cap for gas accumulation may slow down upward ascending gas. The data from the coring sites on this ridge are thus consistent with lower depth-integrated rates of gas dissolution. This result differs from *Chuang et al*. [2010] who calculated sulfate fluxes to the SMT of 418 mmol $m^{-2}$ $yr^{-1}$ for a site on the frontal segment of Tai-Nan Ridge, compared to a flux of only 29 mmol $m^{-2}$ $yr^{-1}$ in this study ($F_{SR}+F_{AOM}$, Table 6). Yet, they sampled above the acoustic turbidity zone where a group of normal faults developed on the eastern flank (Figure 1c), and we argue that normal faults form a

conduit for high rates of methane ascent and accumulation in anticlines, possibly leading to the formation of hydrate or gas deposits. Consequently, we conclude that areas with acoustic turbidity are those with the highest depth-integrated rates of methane turnover, as has been demonstrated for passive margins [*Dale et al*., 2009].

### 7.3. A Deep Source of Biogenic Methane

[58] The methane isotopes indicate a mainly biogenic origin of gas [*Whiticar*, 1999]. In addition, higher hydrocarbons are negligible and $\delta$D-$CH_4$ measured in other cores in the same area range from −160‰ to −240‰ (Yang et al., unpublished data), which further indicate methane generation from microbial $CO_2$ reduction [*Whiticar*, 1999]. The isotope fractionation for methanogenesis can be roughly estimated from the data below the SMT as $\varepsilon = \delta^{13}C\text{-}CO_2 – \delta^{13}C\text{-}CH_4$ = 27 to 47‰ (Figure 3); values which are well within fractionations for biogenic methanogenesis [*Whiticar*, 1999]. The strong depletions in $^{13}C\text{-}CH_4$ at the depth of SMT on all ridges are produced by methanogenesis using $^{13}C$-depleted dissolved $CO_2$ from AOM [*Borowski et al*., 1997]. The enrichment in $^{13}C\text{-}CH_4$ seen through the core on Tai-Nan Ridge could be interpreted as methane production using an increasingly heavy $CO_2$ pool with depth in the sediment [*Claypool and Threlkeld*, 1983; *Borowski et al*., 1997]. However, as predicted by the modeling, the absence of a gradient in $\delta^{13}C\text{-}CO_2$ below the SMT on Tai-Nan and Yung-An ridges seems to indicate insignificant rates of biogenic gas generation in these layers. The variability in $\varepsilon$ between ridges could therefore reflect the different amounts and rates of mixing between deep and shallow gas. Taken together, this implies that the $^{13}C\text{-}CH_4$ enrichment on Tai-Nan Ridge is driven by mixing of gases with different isotopic compositions.

[59] Organic matter buried below sulfate reduction zone is well preserved (Table 6) and accumulates at high depth-integrated rates due to high terrestrial particulate runoff from the Western Foothill and Central Mountain Range of southern Taiwan and subsequent offshore sedimentation velocities are as high as 0.08 cm $yr^{-1}$. Yet, this organic material is apparently unreactive toward methanogenesis in the upper 30 m. Free methane gas of biogenic origin may be generated in deeper sediments if refractive POC becomes primed for degradation by the increase in temperature with sediment depth [*Burdige*, 2011]. Based on heat-flow measurements by *Shyu et al*. [2006], the extrapolated temperature below the BSR offshore SW Taiwan (Site 714htg21) is 18.8°C. Thus, given a geothermal gradient of 38°C $km^{-1}$ and the fact that methanogens can survive at temperatures up to 100°C [*Zinder*, 1993; *Head et al*., 2003], these microorganisms can exist to depths in excess of 2000 m below the BSR. The discovery and extraction of biogenic gas from the Hsinying gas field by the Chinese Petroleum Corporation indicates that free gas is being generated by microorganisms at these depths [*Oung et al*., 2006]. It seems likely that upward transport of gas from these deep sources constitutes the main supply route of biogenic gas that dissolves in the shallow sediments on the three ridges.

### 7.4. Potential Gas Hydrate Formation on Yung-An Ridge

[60] The halogens iodide and bromide can be used to identify and even quantify organic matter mineralization [*Price et al*, 1970; *Shiskina*, 1978; *Martin et al*., 1993], whereas chloride can provide important information on hydrate formation and dissolution and clay mineral dewatering [*Kastner et al*., 1991]. Accordingly, the pore fluid composition of $Cl^-$ and $I^-$ has been used to identify the relative importance of these processes in deep sediments [*Lu et al*., 2008]. Pore water iodide and chloride concentrations from SW Taiwan are plotted in Figure 5 alongside previously published data, including results from ODP coring sites on Cascadia margin [*Lu et al*., 2008]. In general, our data from Tai-Nan and Yung-An Ridge showed no strong signs of clay mineral dehydration and instead cluster around organic matter degradation as the dominant process. However, the iodide data are mainly restricted to the bubble irrigation zones, which somewhat obscures any tendency toward hydrate formation indicated in the chloride profiles at Site MD05-2911.

[61] Two data points in the deeper part of core MD05-2913 on Good Weather Ridge lie between organic matter degradation and clay mineral dehydration pathways. This can be explained by comparison to data from onshore mud volcanoes in SW Taiwan which are also shown in Figure 5. On the basis of heavy $\delta^{11}B$ pore fluids, *Chao et al*. [2011] proposed that these pore fluids are affected by clay mineral dehydration. Due to the progressive eastward subduction of the Eurasian Continental Plate under the Philippine Sea Plate, the signature of the clay mineral dehydration

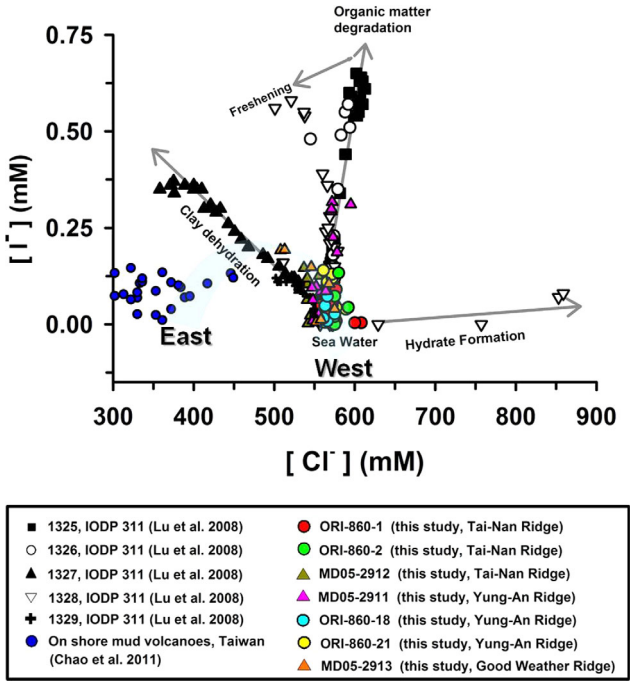


**Figure 5.** Iodide versus chloride concentrations in sediment pore water from near Taiwan (colored symbols) and from an accretionary prism on the Cascadia margin (figure modified from *Lu et al*. [2008]). The east-west arrow refers to the relative locations for on shore mud volcanoes and offshore sampling sites in southwest Taiwan.

generated from subduction compression may be carried into the shallow sediments of the most easterly ridge (Good Weather). Although limited by the little data available, this could explain the shift in pore water composition on Good Weather Ridge in Figure 5 and tentatively supports our assumption that upward fluid flow is of little relevance with regard to methane dynamics on Tai-Nan and Yung-An Ridge, with bubble irrigation being of greater importance. $\delta^{18}O$ and $\delta D$ data of the pore water are required to validate this hypothesis

[62] Observed BSRs throughout the sediments offshore SW Taiwan suggest the presence of free gas underneath hydrate-bearing sediments even though gas hydrates have yet to be recovered with sediment cores. The dissolved methane concentration in equilibrium with gas hydrates ($L_{GH}$) under the in situ conditions of each core was ~64 mM at the study sites [*Tishchenko et al*., 2005, Table 2]. Since the model-predicted methane concentrations are much higher than this in the deep sediment layers at five out of seven sites investigated (Figure 2a), one may expect hydrates to form there. Hydrate formation is also suggested by the moderate chloride enrichment of up to ~600 mM below 2000 cmbsf at Site MD05-2911 on Yung-An Ridge (Figure 2e).

[63] We estimated the potential methane hydrate formation rate at MD05–2911 by simulating the dissolved chloride enrichment by expanding the model to include the following equation for chloride [*Haeckel et al*., 2004]:

$$\Phi \cdot \frac{\partial C(\mathrm{Cl})}{\partial t} = \frac{\partial\left(\Phi \cdot D_{s(\mathrm{Cl})} \cdot \frac{\partial C(\mathrm{Cl})}{\partial x}\right)}{\partial x} - \frac{\partial(\Phi \cdot v \cdot C(\mathrm{Cl}))}{\partial x} + \Phi \cdot R_i + C(\mathrm{Cl}) \cdot \frac{\rho_{GH}}{\rho_{PW}} \cdot R_{GH} \quad (13)$$

where $C(\mathrm{Cl})$ is the chloride concentration, $\rho_{GH}$ (0.9 g $cm^{-3}$) is the gas hydrate density, $\rho_{PW}$ (1.033 g $cm^{-3}$) is the pore water density, and $R_{GH}$ is the rate of methane hydrate formation ($cm^3$ gas hydrate ($cm^3$ bulk sediment)$^{-1}$ $yr^{-1}$). The change in porosity due to hydrate formation is not considered since the potential pore space filled by hydrate is small (see below). The value of $R_{GH}$ is related to the methane concentration in equilibrium with gas hydrate:

$$R_{GH} = k_{GH} \cdot \left(\frac{C(CH_4)}{L_{GH}} - 1\right) \quad \text{for} \left[\left(\frac{C(CH_4)}{L_{GH}}\right) > 1\right] \quad (14)$$

where $k_{GH}$ (units as $R_{GH}$) is the kinetic constant of methane hydrate formation. Thus, gas hydrate formation is only possible when the dissolved

methane concentration exceeds $L_{GH}$. The corresponding expression for methane in equation (1) becomes:

$$\Phi \cdot \frac{\partial C(CH_4)}{\partial t} = \frac{\partial\left(\Phi \cdot D_{s(CH_4)} \cdot \frac{\partial C(CH_4)}{\partial x}\right)}{\partial x} - \frac{\partial(\Phi \cdot v \cdot C(CH_4))}{\partial x} + \Phi \cdot R_c + \Phi \cdot R_i + \frac{\rho_{GH}}{M_{GH}} \cdot R_{GH} \quad (15)$$

where $M_{GH}$ is molecular weight of natural gas hydrate ($M_{GH} = 0.1223$ g mmol$^{-1}$, equivalent to a stoichiometric formula of $CH_4$ . 5.9 $H_2O$.

[64] The chloride enrichment was successfully reproduced using a value of $k_{GH}$ of $2.8\times10^{-5}$ cm$^3$ gas hydrate (cm$^3$ bulk sediment)$^{-1}$ yr$^{-1}$ (Figures 6a and 6b), giving a potential depth-integrated rate of gas hydrate formation of $3.5\times10^{-4}$ mmol $CH_4$ m$^{-2}$ yr$^{-1}$ occupying a pore space of only 0.6 %. For comparison, this depth-integrated rate is at least 9 orders of magnitude lower than at Hydrate Ridge ($10^5$ mmol $CH_4$ m$^{-2}$ yr$^{-1}$, *Torres et al.* [2004]; $1.08\times10^7$ mmol $CH_4$ m$^{-2}$ yr$^{-1}$, *Haeckel et al.* [2004]) and 1 order of magnitude higher than for Site 997 on Blake Ridge (4.3 mmol $CH_4$ m$^{-2}$ yr$^{-1}$, *Egeberg and Dickens* [1999]). Although our model only captures the upper part of the hydrate saturation zone, the elevated rate of hydrate formation rate at Hydrate Ridge results from high rates of upward fluid advection (45–300 cm yr$^{-1}$, *Haeckel et al.* [2004]; 1–10 cm yr$^{-1}$, *Torres et al.* [2004]), whereas on Blake Ridge, it is much lower at 0.01 cm yr$^{-1}$ [*Egeberg and Dickens*, 1999]. Additionally, *Wallmann et al.* [2006a] suggested that hydrate formation on Blake Ridge is sustained by gas bubble ascent and not organic matter degradation within the gas hydrate stability zone.

[65] Other interesting geochemical features related to hydrate dynamics have been detected below 20 mbsf in MD05-2911. For example, *Lim et al.* [2011] reported high concentrations of pyrite (251–380 μmol g$^{-1}$) and $\delta^{13}$C-depleted carbonate (−29‰) which were interpreted as evidence for the SMT paleodepth. Abundant pyrite tubes, authigenic carbonate nodules and $^{13}$C-depleted authigenic carbonates (−54‰ to −46‰) were also described in the same core by *Huang et al.* [2006]. Authigenic carbonates, chloride enrichments and predicted methane concentrations higher than $L_{GH}$ only coexist in core MD05-2911 below 20 mbsf and not in cores MD05-2912 and MD05-2913. This may suggest that authigenic carbonate precipitates during the formation of gas hydrate and enriches the pore

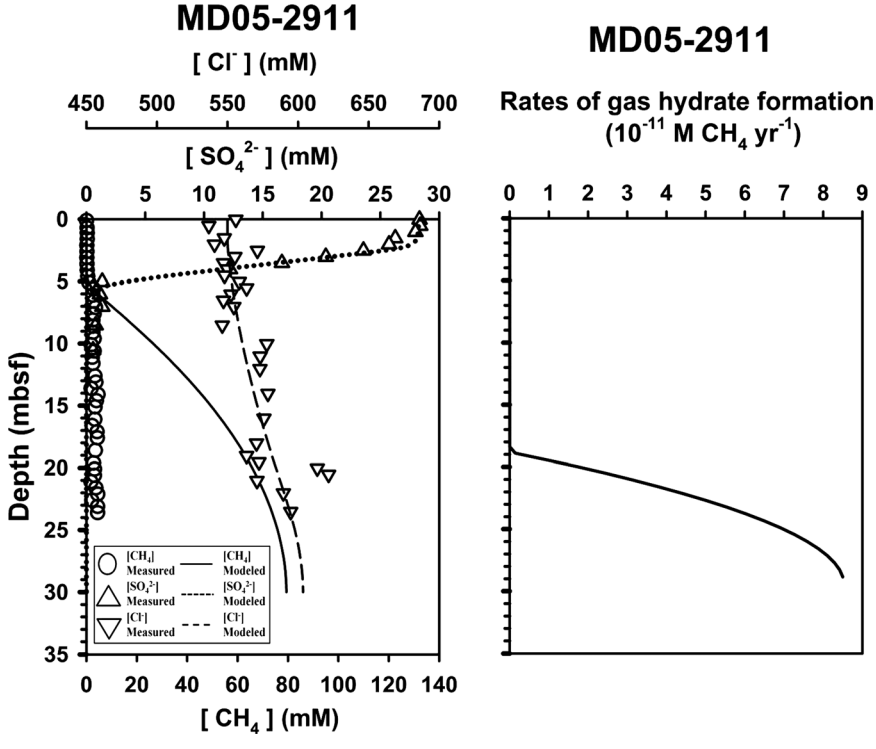


**Figure 6.** Modeled hydrate formation rates in core MD05–2911 on Yung-An Ridge. (a) Depth profiles of sulfate, methane, and chloride concentrations and (b) Rate of gas hydrate formation in $10^{-11}$ M $CH_4$ yr$^{-1}$.

water in calcium and carbonate ions, thus increasing the saturation of calcium carbonate [*Teichert et al*., 2005]. Further studies on contemporary rates of authigenic carbonate precipitation in SW Taiwan are required to validate our modeled hydrate formation rates as well as the use of $^{13}C$-depleted authigenic carbonates as a proxy for SMT paleodepth.

## 8. Conclusions

[66] A numerical model developed for continental margin settings [*Wallmann et al*., 2006a] has been applied to data from 30 m long piston cores sampled in the accretionary wedge offshore SW Taiwan to identify trends in the reactivity of the organic material and to determine the depth-integrated turnover rates of sulfate, methane and POC. BSRs across the region indicate the presence of gas hydrates, although none were recovered from the near-surface sediments of the present study. Sediments in the accretionary wedge were characterized by a poorly reactive POC with the carbon burial fraction ranging from 64 to 89% over the upper 30 m of sediment. The data strongly indicate the presence of a much larger source of methane supplied by gas bubbles rising through the sediment, possibly originating from biogenic methanogenesis below the hydrate stability zone. Dissolution of the gas drives anaerobic methane oxidation coupled to sulfate reduction at depth-integrated rates comparable to other continental shelf settings. There was no evidence for methane transport by upward fluid flow (i.e., fluid expulsion) and, besides, this idea is inconsistent with the sulfate profiles that show characteristic irrigation-like trends caused by rising gas bubbles and pore water-seawater mixing as previously described by *Haeckel et al*. [2007].

[67] The relative importance of these processes, in addition to the reactivity of POC, has been interpreted in the context of the different geological settings of the sampling sites. For example, emergent thrusts may facilitate methane gas migration and accelerate chemical reactions, whereas these rates might be attenuated when the sediments overly blind faults and anticlines. Knowledge of the underling geology in active margin sediments such as offshore SW Taiwan is critical to help interpreting the geochemistry in near-surface sediments as well as deriving regional chemical budgets.

## Acknowledgments

[68] We thank the crew of the R/V *Ocean Research Vessel I* and R/V *Marion Dufresne* and all assistants and students on board for their help in sample collection and preparation. The Central Geological Survey (5226902000-05-94-02; 97-5226904000-04-03) and National Science Council (NSC100-2116-M-002-027; NSC102-3113-P-002-005) of Taiwan, R.O.C. provided financial support for this study. Yue-Gau Chen offered the instruments for sediment POC measurements. J. Wu helped for the iodine analysis in MD cores. Two anonymous reviewers provided constructive comments/suggestions to improve the manuscript. The senior author (PCC) was benefited from the scholarship from NSC-DAAD Sandwich Program for research visits to Germany (NSC99-2911-I-002-053-2).

## References

Albert, D. B., C. S. Martens, and M. J. Alperin (1998), Biogeochemical processes controlling methane in gassy coastal sediments—Part 2: Groundwater flow control of acoustic turbidity in Eckernförde Bay Sediments, *Cont. Shelf Res.*, *18*, 1771–1793.

Algar, C. K., B. P. Boudreau, and M. A. Barry (2011), Initial rise of bubbles in cohesive sediments by a process of viscoelastic fracture, *J. Geophys. Res.*, *116*, B04207, doi:10.1029/2010JB008133.

Alperin, M. J., and T. M. Hoehler (2009), Anaerobic methane oxidation by archaea/sulfate-reducing bacteria aggregates: 1. Thermodynamic and physical constraints, *Am. J. Sci.*, *309*, 869–957, doi:10.2475/10.2009.01.

Barnes, R. O., and E. D. Goldberg (1976), Methane production and consumption in anoxic marine sediments, *Geology*, *4*, 297–300.

Berner, R. A. (1980), *Early Diagenesis—A Theoretical Approach*, Princeton Univ. Press, Princeton, N. J.

Borowski, W. S., C. K. Paull, and W. Ussler III (1996), Marine pore water sulfate profiles indicate in situ methane flux from underlying gas hydrate, *Geology*, *24*, 655–658, doi:10.1130/0091-7613(1996)024<0655:MPWSPI>2.3.CO;2.

Borowski, W. S., C. K. Paull, and W. Ussler III (1997), Carbon cycling within the upper methanogenic zone of continental-rise sediments: An example from the methane-rich sediments overlying the Blake Ridge gas hydrate deposits, *Mar. Chem.*, *57*, 299–311, doi:10.1016/S0304-4203(97)00019-4.

Boudreau, B. P. (1997), *Diagenetic Models and Their Implementation. Modelling Transport and Reactions in Aquatic Sediments*, 414 pp., Springer-Verlag, Berlin.

Briggs, B. R., J. W. Pohlman, M. Torres, M. Riedel, E. L. Brodie, and F. S. Colwell (2011), Macroscopic biofilms in fracture-dominated sediment that anaerobically oxidize methane, *Appl. Environ. Microbiol.*, *77*, 6780–6787, doi:10.1128/AEM.00288-11.

Burdige, D. J. (2007), Preservation of organic matter in marine sediments: Controls, mechanisms, and an imbalance in sediment organic carbon budgets?, *Chem. Rev.*, *107*, 467–485, doi:10.1021/cr050347q.

Burdige, D. J. (2011), Temperature dependence of organic matter remineralization in deeply-buried marine sediments, *Earth Planet. Sci. Lett.*, *311*, 396–410, doi:10.1016/j.epsl.2011.09.043.

Chao, H. C., C. F. You, B. S. Wang, C. H. Chung, and K. F. Huang (2011), Boron isotopic composition of mud volcano fluids: Implications for fluid migration in shallow subduction zones, *Earth Planet. Sci. Lett.*, *305*, 32–44, doi:10.1016/j.epsl.2011.02.033.

Chi, W. C., D. L., Reed, C. S. Liu, and N. Lunberg (1998), Distribution of the bottom simulating reflector in the offshore Taiwan collision zone, *Terr. Atmos. Oceanic Sci.*, *9*, 779–793.

Chiu, J. K., W. H. Tseng, and C. S. Liu (2006), Distribution of gassy sediments and mud volcanoes offshore southwestern Taiwan, *Terr. Atmos. Oceanic Sci.*, *17*, 703–722.

Chuang, P. C., T. F. Yang, S. Lin, H. F. Lee, T. F. Lan, W. L. Hong, C. S. Liu, J. C. Chen, and Y. Wang (2006), Extremely high methane concentration in bottom water and cored sediments from offshore southwestern Taiwan, *Terr. Atmos. Oceanic Sci.*, *17*, 903–920.

Chuang, P. C., T. F. Yang, W. L. Hong, S. Lin, C. H. Sun, A. T.-S. Lin, J. C. Chen, Y. Wang, and S. H. Chung (2010), Estimation of methane flux offshore SW Taiwan and the influence of tectonics on gas hydrate accumulation, *Geofluids*, *10*, 497–510, doi:10.1111/j.1468-8123.2010.00313.x.

Claypool, G. E., and C. N. Threlkeld (1983), Anoxic diagenesis and methane generation in sediments of the Blake Outer Ridge, Deep Sea Drilling Project Site 533, Leg 76, in *Initial Reports DSDP*, vol. *76*, edited by R. E. Sheridan, et al., pp. 391–402, U.S. Gov. Print. Off., Wash.

Coffin, R. B., L. Hamdan, R. J. PlummerSmith, J. Gardner, and W. T. Wood (2008), Analysis of methane and sulfate flux in methane charged sediments from the Mississippi Canyon, Gulf of Mexico, *Mar. Pet. Geol.*, *25*, 977–987, doi:10.1016/j.marpetgeo.2008.01.014.

Dale, A. W., P. Regnier, N. J. Knab, B. B. Jørgensen, and P. Van Cappellen (2008), Anaerobic oxidation of methane (AOM) in marine sediments from the Skagerrak (Denmark): II. Reaction-transport modelling, *Geochim. Cosmochim. Acta*, *72*, 2880–2894, doi:10.1016/j.gca.2007.11.039.

Dale, A. W., P. Regnier, P. Van Cappellen, H. Fossing, J. B. Jensen, and B. B. Jorgensen (2009), Remote quantification of methane fluxes in gassy marine sediments through seismic survey, *Geology*, *37*, 235–238, doi:10.1130/G25323A.1.

Dale, A. W., S. Sommer, M. Haeckel, K. Wallmann, P. Linke, G. Wegener, and O. Pfannkuche (2010), Pathways and regulation of carbon, sulfur and energy transfer in marine sediments overlying methane gas hydrates on the Opouawe Bank (New Zealand), *Geochim. Cosmochim. Acta*, *74*, 5763–5784, doi:10.1016/j.gca.2010.06.038.

Dickens, G. R. (2001), Sulfate profiles and barium fronts in sediment on the Blake Ridge: Present and past methane fluxes through a large gas hydrate reservoir, *Geochim. Cosmochim. Acta*, *65*, 529–543, doi:10.1016/S0016-7037(00)00556-1.

Duan, Z., N. Møller, J. Greenberg and J. H. Weare (1992a), The prediction of methane solubility in natural waters to high ionic strength from 0 to 250°C and from 0 to 1600 bar, *Geochim. Cosmochim. Acta*, *56*, 1451–1460, doi:10.1016/0016–7037(92)90215-5.

Duan, Z., N. Møller, and J. H. Weare (1992b), An equation of state for the $CH_4$-$CO_2$-$H_2O$ system: I. Pure systems from 50 to 1000°C and 0 to 8000 bar, *Geochim. Cosmochim. Acta*, *56*, 2605–2617, doi:10.1016/S0016-7037(02)01226-7.

Egeberg, P. K., and G. R. Dickens (1999), Thermodynamics and pore water halogen constraints on gas hydrate distribution at ODP Site 997 (Blake Ridge), *Chem. Geol.*, *153*, 53–79, doi:10.1016/S0009-2541(98)00152-1.

Feseker, T., K. R. Brown, C. Blanchet, F. Scholz, M. Nuzzo, A. Reitz, M. Schmidt, and C. Hensen (2010), Active mud volcanoes on the upper slope of the western Nile deep-sea fan-first results from the P362/2 cruise of R/V Poseidon, *Geo-Mar. Lett.*, *30*, 169–186, doi:10.1007/s00367-010-0192-0.

Fossing H., T. G. Ferdelman, and P. Berg (2000), Sulfate reduction and methane oxidation in continental margin sediments influenced by irrigation (South-East Atlantic off Namibia), *Geochim. Cosmochim. Acta*, *64*, 897–910, doi:10.1016/S0016–7037(99)00349-X.

Haeckel, M., E. Suess, K. Wallmann, and D. Rickert, (2004), Rising methane gas bubbles form massive hydrate layers at the seafloor, *Geochim. Cosmochim. Acta*, *68*, 4335–4354, doi:10.1016/j.gca.2004.01.018.

Haeckel, M., K. Wallmann, and B. P. Boudreau (2007), Bubble-induced porewater mixing: A 3-D model for deep porewater irrigation, *Geochim. Cosmochim. Acta*, *71*, 5135–5154, doi:10.1016/j.gca.2007.08.011.

Head, I. M., D. M. Jones, and S. R. Larter (2003), Biological activity in the deep subsurface and the origin of heavy oil, *Nature*, *426*, 344–352, doi:10.1038/nature02134.

Henkel, S., et al. (2011), An interdisciplinary investigation of a recent submarine mass transport deposit at the continental margin off Uruguay, *Geochem. Geophys. Geosyst.*, *12*, Q08009, doi:10.1029/2011GC003669.

Hensen, C., M. Zabel, K. Pfeifer, T. Schwenk, S. Kasten, N. Riedinger, H. D. Schulz, and A. Boetius (2003), Control of sulfate pore-water profiles by sedimentary events and the significance of anaerobic oxidation of methane for the burial of sulfur in marine sediments, *Geochim. Cosmochim. Acta*, *67*, 2631–2647, doi:10.1016/S0016–7037(03)00199-6.

Hesse, R., and W. E. Harrison (1981), Gas hydrates (clathrates) causing porewater freshening and oxygen isotope fractionation in deep-water sedimentary sections of terrigenous continental margins, *Earth Planet. Sci. Lett.*, *55*, 453–462, doi:10.1016/0012–821X(81)90172-2.

Holbrook, W. S., H. Hoskins, W. T. Wood, R. A. Stephen, and D. Lizarralde (1996), Methane hydrate and free gas on the Blake Ridge from vertical seismic profiling, *Science*, *273*, 1840–1843, doi:10.1126/science.273.5283.1840.

Holmkvist L., T. G. Ferdelman, and B. B. Jørgensen (2011), A cryptic sulfur cycle driven by iron in the methane zone of marine sediment (Aarhus Bay, Denmark), *Geochim. Cosmochim. Acta*, *75*, 3581–3599. doi:10.1016/j.gca.2011.03.033.

Huang, C. Y., W. Y. Wu, C. P. Chang, S. Tsao, P. B. Yuan, C. W. Lin, and K. Y. Xia (1997), Tectonic evolution of accretionary prism in the arc-continent collision terrane of Taiwan, *Tectonophysics*, *281*, 31–51, doi:10.1016/S0040-1951(97)00157-1.

Huang, C. Y., C. W. Chien, M. Zhao, H. C. Li, and Y. Iizuka (2006), Geological study of active cold seeps in the syn-collision accretionary prism Kaoping slope off SW Taiwan, *Terr. Atmos. Oceanic Sci.*, *17*, 679–702.

Hyndman, R. D., and E. E. Davis (1992), A mechanism for the formation of methane hydrate and seafloor bottom-simulating reflectors by vertical fluid expulsion, *J. Geophys. Res.*, *97*, 7125–7041, doi:10.1029/91JB03061.

Jørgensen, B. B., and D. C. Nelson (2004), Sulfur biogeochemistry—Past and present, in *Sulfide Oxidation in Marine Sediments: Geochemistry Meets Microbiology*, vol. *379*, edited by J. P. Amend et al., pp. 63–81, Geological Society of America Special Paper. Geological Society of America, Boulder, Colorado.

Jørgensen, B. B., and S. Kasten (2006), Sulfur cycling and methane oxidation, in *Marine Geochemistry*, 2nd ed., edited by H. D. Schulz, and M. Zabel, pp. 271–309, Springer, Berlin.

Kastner, M., H. Elderfield, and J. B. Martin (1991), Fluids in convergent margins: What do we know about their composition, origin, role in diagenesis and importance for oceanic chemical fluxes?, *Philos. Trans. R. Soc.*, *335*, 243–259, doi:10.1098/rsta.1991.0045.

Kvenvolden, K. A. (1993), Gas hydrates—Geological perspective and global change, *Rev. Geophys.*, *31*, 173–187, doi:10.1029/93RG00268.

Kvenvolden, K. A. (1998), A primer on the geological occurrence of gas hydrate, in *Gas Hydrates: Relevance to World Margin*

*Stability and Climate Change*, vol. 137, edited by J. P. Henriet and J. Mienert, pp. 9–30, the Geological Society, London.

Lee, H. F., T. F. Yang, T. F. Lan, S. R. Song, and S. Tsao (2005), Fumarolic gas composition of the Tatun Volcano Group, northern Taiwan, *Terr. Atmos. Oceanic Sci.*, *16*, 843–864.

Lee, H. F., T. F. Yang, T. F. Lan, C. H. Chen, S. R. Song, and S. Tsao (2008), Temporal variations of gas compositions of fumaroles in the Tatun Volcano Group, northern Taiwan, *J. Volcanol. Geotherm. Res.*, *178*, 624–635, doi:10.1016/j.jvolgeores.2008.06.005.

Lim, Y. C., S. Lin, T. F. Yang, Y. G. Chen, and C. S. Liu (2011), Variations of methane induced pyrite formation in the accretionary wedge sediments offshore southwestern Taiwan, *Mar. Pet. Geol.*, *28*, 1829–1837, doi:10.1016/j.marpetgeo.2011.04.004.

Lin, A. T., C. S. Liu, C. C. Lin, P. Schnürle, G. Y. Chen, W. Z. Liao, L. S. Teng, H. R. Chuang, and M. S. Wu (2008), Tectonic features associated with the overriding of an accretionary wedge on top of a rifted continental margin: An example from Taiwan, *Mar. Geol.*, *255*, 186–203, doi:10.1016/j.margeo.2008.10.002.

Lin, C. C., A. T. Lin, C. S. Liu, G. Y. Chen, W. Z. Liao, and P. Schnürle (2009), Geological controls on BSR occurrences in the incipient arc-continent collision zone off southwest Taiwan, *Mar. Pet. Geol.*, *26*, 1118–1131, doi:10.1016/j.marpetgeo.2008.11.002.

Lin, S., W. C. Hsieh, Y. C. Lim, T. F. Yang, C. S. Liu, and Y. Wang (2006), Methane migration and its influence on sulfate reduction in Good Weather Ridge region, South China Sea continental margin sediments, *Terr. Atmos. Oceanic Sci.*, *17*, 883–902.

Lin, S., Y. C. Lim, T. F. Yang, S. H. Chung, and Y. Wang (2009), Proxy of past and present methane migration in the active accreted continental margin sediments offshore southwestern Taiwan, *Geochim. Cosmochim. Acta*, *73*(13), A767, Suppl. 1.

Liu, C. S., I. L. Huang, and L. S. Teng (1997), Structural features off southwestern Taiwan, *Mar. Geol.*, *137*, 305–319, doi:10.1016/S0025–3227(96)00093-X.

Liu, C. S., S. Y. Liu, S. Lallemand, N. Lundberg, and D. L. Reed (1998), Digital elevation model offshore Taiwan and its tectonic implication, *Terr. Atmos. Oceanic Sci.*, *9*, 705–738.

Liu, C. S., B. Deffontaines, C. Y. Lu, and S. Lallemand (2004), Deformation patterns of an accretionary wedge in transition zone from subduction to collision offshore southwestern Taiwan, *Mar. Geophys. Res.*, *25*(1–2), 123–137, doi:10.1007/s11001-005-0738-0.

Liu, C. S., P. Schnürle, Y. Wang, S. H. Chung, S. C. Chen, and T. H. Hsiuan (2006), Distribution and characters of gas hydrate offshore of southwestern Taiwan, *Terr. Atmos. Oceanic Sci.*, *17*, 615–644.

Lu, Z., C. Hensen, U. Fehn, and K. Wallmann (2008), Halogen and $^{129}I$ systematics in gas hydrate fields at the northern Cascadia margin (IODP Expedition 311): Insights from numerical modeling, *Geochem. Geophys. Geosyst.*, *9*, Q10006, doi:10.1029/2008GC002156.

Martens, C. S. (1976), Control of methane sediment-water bubble transport by macroinfaunal irrigation in Cape Lookout Bight, North Carolina, Science, *192*, 998–1000, doi:10.1126/science.192.4243.998.

Martin, J. B., J. M. Gieskes, M. Torres, and M. Kastner (1993), Bromine and iodine in Peru margin sediments and pore fluids: Implications for fluid origins, *Geochim. Cosmochim. Acta*, *57*, 4377–4389, doi:10.1016/0016–7037(93)90489-J.

Marquardt, M., C. Hensen, E. Pinero, K. Wallmann, and M. Haeckel (2010), A transfer function for the prediction of gas hydrate inventories in marine sediments, *Biogeosciences*, *7*, 2925–2941, doi:10.5194/bg-7–2925-2010.

Meyers, P. A. (1994), Preservation of elemental and isotopic source identification of sedimentary organic matter, *Chem. Geol.*, *114*, 289–302, doi:10.1016/0009–2541(94)90059-0.

Middelburg, J. J. (1989), A simple model for organic matter decomposition in marine sediments, *Geochim. Cosmochim. Acta*, *53*, 1577–1581, doi:10.1016/0016–7037(89)90239-1.

Milkov, A. V. (2004), Global estimates of hydrate-bound gas in marine sediments: How much is really out there?, *Earth Sci. Rev.*, *66*, 183–197, doi:10.1016/j.earscirev.2003.11.002.

Niewöhner, C., C. Hensen, S. Kasten, M. Zabel, and H.D. Schulz (1998), Deep sulfate reduction completely mediated by anaerobic methane oxidation in sediments of the upwelling area off Namibia, *Geochim. Cosmochim. Acta*, *62*, 455–464, doi:10.1016/S0016–7037(98)00055-6.

Oung, J., C. Y. Lee, C. S. Lee, and C. Kuo, (2006), Geochemical study on hydrocarbon gases in seafloor sediments, southwestern offshore Taiwan—Implications in the potential occurrence of gas hydrates, *Terr. Atmos. Oceanic Sci.*, *17*(4), 921–931.

Paull, C. K., T. D. Lorenson, G. Dickens, W. S. Borowski, W. Ussler III, and K. A. Kvenvolden (2000), Comparison of in situ and core gas measurements in ODP Leg 164 bore holes, in *Gas Hydrates: Challenges for the Future,* vol. 912, edited by G. D. Holder and P. R. Bishnoi, pp. 23–31, New York Academy of Sciences, New York.

Price, N. B., S. E. Calvert, and P. G. W. Jones (1970), The distribution of iodine and bromine in recent sediments of the southwestern Barents Sea, *J. Mar. Res.*, *28*, 22–34.

Reed, D. L., N. Lundberg, C. S. Liu, and B. Y. Kuo (1992), Structural relations along the margins of the offshore Taiwan accretionary wedge: Implications for accretion and crustal kinematics, *Acta Geol. Taiwan.*, *30*, 105–122.

Regnier, P., A. W. Dale, S. Arndt, D. E. LaRowe, J. M. Mogollón, and P. Van Cappellen (2011), Quantitative analysis of anaerobic oxidation of methane (AOM) in marine sediments: A modelling perspective, *Earth-Sci. Rev.*, *106*, 105–130, doi:10.1016/j.earscirev.2011.01.002.

Schmidt, M., C. Hensen, T. Mörz, C. Müller, I. Grevemeyer, K. Wallmann, S. Mau, and N. Kaul (2005), Methane hydrate accumulation in "Mound 11" mud volcano, Costa Rica forearc, *Mar. Geol.*, *216*, 77–94, doi:10.1016/j.margeo.2005.01.001.

Schulz, H. D., A. Dahmke, U. Schinzel, K. Wallmann, and M. Zabel (1994), Early diagenetic processes, fluxes, and reaction rates in sediments of the South Atlantic, *Geochim. Cosmochim. Acta*, *58*, 2041–2060, doi:10.1016/0016–7037(94)90284-4.

Schwalenberg, K., M. Haeckel, J. Poort, and M. Jegen (2010), Evaluation of gas hydrate deposits in an active seep area using marine controlled source electromagnetics: Results from Opouawe Bank, Hikurangi Margin, New Zealand, *Mar. Geol.*, *272*, 79–88, doi:10.1016/j.margeo.2009.07.006.

Shiskina, O. V. (1978), Distribution of bromine, Cl/Br relationships, and iodine in interstitial water of the Black Sea, based on DSDP Leg 42B, in *Initial Reports, DSDP 42, Pt. 2*, edited by D. A. Ross et al., pp. 631–635, U.S. Gov. Print. Off., Washington, D. C.

Shyu, C. T., Y. J. Chen, S. T. Chiang, and C. S. Liu (2006), Heat flow measurements over bottom simulating reflectors, offshore southwestern Taiwan, *Terr. Atmos. Oceanic Sci.*, *17*, 845–869.

Suess, E., B. Carson, S. D. Ritger, J. C. Moore, M. L. Jones, G. R. Kulm, and G. R. Cochrane (1985), Biological communities at vent sites along the subduction zone off Oregon, in

*The Hydrothermal Vents of the Eastern Pacific: An Overview*, vol. 6, edited by M. L. Jones, pp. 475–484, Bull. of the Biol. Soc. of Washington.

Suess, E., et al. (1999), Gas hydrate destabilization: Enhanced dewatering, benthic material turnover and large methane plumes at the Cascadia convergent margin, *Earth Planet. Sci. Lett.*, *170*, 1–15, doi:10.1016/S0012-821X(99)00092-8.

Sun, C. H., S. C. Chang, C. L. Kuo, J. C. Wu, P. H. Shao, and J. N. Oung (2010), Origins of Taiwan's mud volcanoes: Evidence from geochemistry, *J. Asian Earth Sci.*, *37*, 105–116, doi:10.1016/j.jseaes.2009.02.007.

Teichert, B. M. A., N. Gussone, A. Eisenhauer, and G. Bohrmann (2005), Clathraites: Archives of near-seafloor pore-fluid evolution ($\delta^{44/40}$Ca, $\delta^{13}$C, $\delta^{18}$O) in gas hydrate environments, *Geology*, *33*, 213–216, doi:10.1130/G21317.1.

Teng, L. S. (1990), Geotectonic evolution of late Cenozoic arc-continent collision in Taiwan, *Tectonophysics*, *183*, 57–76, doi:10.1016/0040-1951(90)90188-E.

Thullner, M., A. W. Dale, and P. Regnier (2009), Global-scale quantification of mineralization pathways in marine sediments: A reaction transport modeling approach, *Geochem. Geophys., Geosyst.*, *10*, Q10012, doi:10.1029/2009GC002484.

Tishchenko, P., C. Hensen, K. Wallmann, and C. S. Wong (2005), Calculation of the stability and solubility of methane hydrate in seawater, *Chem. Geol.*, *219*, 37–52, doi:10.1016/j.chemgeo.2005.02.008.

Torres, M. E., K. Wallmann, A. M. Trehu, G. Bohrmann, W. S. Borowski, and H. Tomaru (2004), Gas hydrate growth, methane transport, and chloride enrichment at the southern summit of Hydrate Ridge, Cascadia margin off Oregon, *Earth Planet. Sci. Lett.*, *226*, 225–241, doi:10.1016/j.epsl.2004.07.029.

Treude, T., A. Boetius, K. Knittel, K. Wallmann, and B. B. Jørgensen (2003), Anaerobic oxidation of methane above gas hydrates at Hydrate Ridge, NE Pacific Ocean, *Mar. Ecol. Prog. Ser.*, *264*, 1–14, doi:10.3354/meps264001.

Tryon, M. D., P. Henry, M. N. Çağatay, T. A. C. Zitter, L. Géli, L. Gasperini, P. Burnard, S. Bourlange, and C. Grall (2010), Pore fluid chemistry of the North Anatolian Fault Zone in the Sea of Marmara: A diversity of sources and processes, *Geochem. Geophys. Geosyst.*, *11*, Q0AD03, doi:10.1029/2010GC003177.

Wallmann, K., G. Aloisi, M. Haeckel, A. Obzhirov, G. Pavlova, and P. Tishchenko (2006a), Kinetics of organic matter degradation, microbial methane generation and gas hydrate formation in anoxic marine sediments, *Geochim. Cosmochim. Acta*, *70*, 3905–3927, doi:10.1016/j.gca.2006.06.003.

Wallmann, K., M. Drews, G. Aloisi, and G. Bohrmann (2006b), Methane discharge into the Black Sea and the global ocean via fluid flow through submarine mud volcanoes, *Earth Planet. Sci. Lett.*, *248*, 544–559, doi:10.1016/j.epsl.2006.06.026.

Westrich, J. T., and R. A. Berner (1984), The role of sedimentary organic matter in bacterial sulfate reduction. The p model tested, *Limnol. Oceanogr.*, *29*, 236–249.

Whiticar, M. J. (1999), Carbon and hydrogen isotope systematics of bacterial formation and oxidation of methane, *Chem. Geol.*, *161*, 291–314, doi:10.1016/S0009-2541(99)00092-3.

Yang, T. F. (2008), Recent progress in the application of gas geochemistry: Examples from Taiwan and the 9th International Gas Geochemistry Conference, *Geofluids*, *8*, 219–229, doi:10.1111/j.1468-8123.2008.00232.x.

Yang, T. F., C. Y. Chou, C. H. Chen, L. L. Chyi, and J. H. Jiang (2003), Exhalation of radon and its carrier gases in SW Taiwan, *Radiat. Meas.*, *36*, 425–429, doi:10.1016/S1350-4487(03)00164-1.

Yang, T. F., G. H. Yeh, C. C. Fu, C. C. Wang, T. F. Lan, H. F. Lee, C. H. Chen, V. Walia, and Q. C. Sung (2004), Composition and exhalation flux of gases from mud volcanoes in Taiwan, *Environ. Geol.*, *46*, 1003–1011, doi:10.1007/s00254-004-1086-0.

Yang, T. F., P. C. Chuang, S. Lin, J. C. Chen, Y. Wang, and S. H. Chung (2006), Methane venting in gas hydrate potential area offshore of SW Taiwan: Evidence of gas analysis of water column samples, *Terr. Atmos. Oceanic Sci.*, *17*, 933–950.

Yeh, G. H., T. F. Yang, J. C. Chen, Y. G. Chen, and S. R. Song (2005), Fluid geochemistry of mud volcanoes in Taiwan, in *Mud Volcanoes, Geodynamics and Seismicity*, edited by G. Martinelli and B. Panahi, pp. 227–237, Springer, Amsterdam.

You, C. F., J. M. Gieskes, T. Lee, T. F. Yui, and H. W. Chen (2004), Geochemistry of mud volcano fluids in the Taiwan accretionary prism, *Appl. Geochem.*, *19*, 695–707, doi:10.1016/j.apgeochem.2003.10.004.

Zabel, M., and H. D. Schulz (2001), Importance of submarine landslides for non-steady state conditions in pore water systems—lower Zaire (Congo) deep-sea fan, *Mar. Geol.*, *176*, 87–99, doi:10.1016/S0025-3227(01)00164-5.

Zinder, S. H. (1993), Physiological ecology of methanogens, in *Methanogenesis Ecology, Physiology, Biochemistry, and Genetic*, edited by J. G. Ferry, pp. 128–206, Chapman and Hall, New York.